An Analytical Model for the Influence of Soil Moisture on Temperature Extremes in the Midlatitudes

ADAM MICHAEL BAUER,[a,b] LUCAS R. VARGAS ZEPPETELLO,[c] AND CRISTIAN PROISTOSESCU[d,e]

[a] Department of Physics, University of Illinois Urbana–Champaign, Urbana, Illinois
[b] Department of the Geophysical Sciences, University of Chicago, Chicago, Illinois
[c] Department of Earth and Planetary Science, University of California, Berkeley, Berkeley, California
[d] Department of Climate, Meteorology, and Atmospheric Sciences, University of Illinois Urbana–Champaign, Urbana, Illinois
[e] Department of Earth Sciences and Environmental Change, University of Illinois Urbana–Champaign, Urbana, Illinois

(Manuscript received 25 October 2024, in final form 1 October 2025, accepted 14 October 2025)

ABSTRACT: Heat waves are expected to increase in severity and frequency under climate change. Case studies have shown that heat waves typically occur during a coalescence of anomalous atmospheric and land surface conditions, but teasing apart the different contributing factors is a challenge, in part owing to the difficulty in disentangling the role of soil moisture from that of atmospheric variations in solar radiation and thermal advection. Here, we provide evidence that low soil moisture is associated with extremely high temperatures in the midlatitudes and develops a theoretical framework to understand this association. We first show that a nonlinear relationship between soil moisture and temperature arises from energy and mass conservation at the land surface and then employ this relationship to quantify the influence of soil moisture on temperature variability. After deriving a diagnostic equation for the nonlinear temperature response to soil moisture variations, we obtain a dynamical Hasselmann-like model for the soil moisture variations themselves. We find that soil moisture fluctuations control the frequency of temperature extremes by slowly altering the land surface climate state on which atmospheric variability is superimposed, rather than by altering atmospheric variability itself. Our diagnostic model allows us to quantify how extreme an atmospheric anomaly needs to be to create a heat wave, conditional on the underlying soil moisture. By forcing our Hasselmann-like model for soil moisture with stochastic precipitation, we derive analytical solutions for the statistical moments of soil moisture.

SIGNIFICANCE STATEMENT: Heat waves strain numerous aspects of human and natural systems. Here, we present an analytical, minimal complexity model to understand how each of these factors contributes to heat waves in the midlatitudes. Our model yields two novel theoretical insights: 1) a nonlinear diagnostic equation for surface temperatures in terms of surface soil moisture content and 2) a nonlinear Hasselmann-like model for the soil moisture response to precipitation. We further show that the strength of this nonlinearity controls the heterogeneous influence of soil moisture on temperature extremes. Our model provides a conceptual understanding of how "fast" atmospheric variability and "slow" variability in land hydrology jointly contribute to temperature extremes in the midlatitudes.

KEYWORDS: Extreme events; Climate change; Climate variability; Soil moisture

1. Introduction

Heat waves heavily impact economies (García-León et al. 2021), ecosystems (Sippel et al. 2016), and human health (Robine et al. 2008); the European heat wave of 2003 alone is estimated to have killed over 70 000 people. These extreme heat events are expected to become more widespread in a warming climate, as changes in both the mean and variance of local temperature distributions are expected to lead to more instances where historical temperature benchmarks are breached (IPCC 2021). Absent adaptation, these extreme events could lead to substantive harm on human and natural systems alike (Carleton and Hsiang 2016; Sun et al. 2024).

As fossil fuel emissions lead to rising global average temperatures, local average temperatures, too, shift toward warmer conditions and lead to more frequent and severe heat waves (Rhines and Huybers 2013). While the precise impact of a warming climate on extreme events is highly sensitive to the details of the underlying distribution (Huybers et al. 2014), a recent study found that the growth rate of local median temperatures scale similarly to local extremely high temperatures, though extremely cold temperatures seem to grow at a comparatively lower rate (McKinnon et al. 2024). A short and nonstationary observational record makes it difficult to robustly estimate how often a given historical temperature threshold should be exceeded locally as the global average temperature rises, though recent work has suggested that bulk hemispheric statistics and the spatiotemporal pattern of temperature extremes provide robust upward trends in local temperature extremes attributable to a rising average global temperature (Van Loon and Thompson 2023; Patel et al. 2024).

Supplemental information related to this paper is available at the Journals Online website: https://doi.org/10.1175/JCLI-D-24-0624.s1.

Corresponding author: Adam Michael Bauer, ambauer@uchicago.edu

DOI: 10.1175/JCLI-D-24-0624.1

A number of studies aim to quantify how much climate change contributes to the likelihood of individual extreme events. However, statistical approaches to attribution depend on fitting the limited number of observations to a given distribution with a number of free parameters (such as a generalized extreme value distribution, which has four free parameters), making it difficult to assign a likelihood to even well-characterized events such as the 2021 Pacific Northwest heat wave (Philip et al. 2022; McKinnon and Simpson 2022). In light of this limitation, recent work has utilized operational weather forecasting models to quantify the human influence on extreme events, including the Pacific Northwest heat wave (Leach et al. 2024), though these approaches rely on running expensive computational models.

In addition to changing the average of local temperature distributions, climate models mostly show increasing temperature variance in the tropics as global temperatures rise (Vargas Zeppetello and Battisti 2020), but there remains considerable intermodel uncertainty (Chan et al. 2022). Furthermore, model biases make comparison across models difficult (Vargas Zeppetello and Battisti 2020). These biases, in addition to limitations in the empirical record mentioned above, highlight a growing need for a unified theory of present-day heat waves, especially outside the tropics (Byrne 2021; Zhang et al. 2021; Byrne et al. 2024).

A full understanding of heat waves, however, has been hampered by the difficulty in disentangling contributing mechanisms that act across a breadth of time scales: atmospheric energetics and blocking patterns (Pfahl and Wernli 2012; Zhang and Boos 2023), cloud variability (Meehl and Tebaldi 2004), and thermal advection near the surface (Schneider et al. 2015; Tamarin-Brodsky et al. 2020) contribute to fast variations in near-surface temperature relative to soil moisture dynamics (Koster and Suarez 2001; Seneviratne et al. 2006b; Lorenz et al. 2010; Vargas Zeppetello et al. 2022). This tension between atmospheric dynamics-centric approaches to analyzing heat waves and surface thermodynamic-centric approaches is thoroughly explored in Duan et al. (2024). Throughout this paper, we will refer to the relatively fast processes (variations in atmospheric energy convergence, thermal advection, and cloud radiative effects) as the "atmospheric forcing" in contrast to variations driven by (comparatively) slower fluctuations in soil moisture. Capturing the interaction of these mechanisms is a key component of any physical theory of heat waves, as it is a general property of stochastic systems that the shape of nonnormal distributional tails is controlled by the interaction of mechanisms across time scales (Proistosescu et al. 2016).

A generic picture of how atmospheric circulation contributes to generating a midlatitude summer "heat dome" involves the spatial stagnation of a high pressure system, known as a "blocking" event. Anticyclonic circulation leads to enhanced surface warming through a combination of subsidence-driven adiabatic heating (Pfahl and Wernli 2012), advection of warm air (Schumacher et al. 2019), and suppression of convection and clouds (Bieli et al. 2015). Each of these mechanisms increases the energy in the boundary layer and, by extension, the temperature near the land surface.

While this excess of energy inevitably warms the surface, it does not necessarily lead to the onset of extremely high temperatures (or a heat wave). Instead, the extent to which increased surface forcing leads to extreme temperatures is modulated by the thermodynamic state of the surface; the surface energy balance, in turn, is modulated by an upper bound on the equivalent potential temperature that, once exceeded, triggers storm activity aloft that cools the surface via injecting moisture back into the soil column (Sherwood and Huber 2010; Buzan and Huber 2020; Zhang and Boos 2023). The land surface thermodynamic state controls the partitioning of incoming atmospheric forcing into two channels: an evapotranspiration (ET) channel, where incoming energy evaporates moisture from the soil column and leads plants to transpire water, and a heating channel, where incoming energy raises temperatures (Seneviratne et al. 2010). Partitioning between these two channels influences near-surface air temperatures and is controlled mainly by two factors: 1) the atmospheric vapor pressure deficit (VPD) and 2) the available moisture in the soil for ET (Budyko 1961; Manabe 1969; Sellers et al. 1997). This partitioning has been shown to exert a strong control on the distribution of temperature extremes (both hot and cold) in reanalysis and climate models (McKinnon et al. 2024). The influence of soil moisture on individual heat waves has been shown in a number of case studies (e.g., Whan et al. 2015), and the link between precipitation deficits (a proxy for dry soils) and extremely hot days has been shown to be widespread (Mueller and Seneviratne 2012). However, a theoretical model of how soil moisture interacts with higher frequency atmospheric variability to influence heat waves is lacking.

In this paper, we first use observational data to demonstrate the relationship between soil moisture and temperature extremes across the continental midlatitudes. With this as a foundation, we use a long reanalysis product to demonstrate the time-scale separation between (slow) soil moisture and (fast) atmospheric variability. We begin our theoretical analysis by developing an idealized model to show how nonlinear coupling between soil moisture and temperature arises out of simple energy and mass balance at Earth's land surface, move from the generic to the specific, and build on a previous framework (Vargas Zeppetello et al. 2022) to quantify soil moisture's influence on temperature variability. Along the way, we explain how "breakpoints" emerge in observations of temperature and soil moisture (Benson and Dirmeyer 2021) in purely physical terms; these breakpoints are by-products of the nonlinear coupling between soil moisture and temperature. Finally, we derive analytical expressions for the soil moisture distribution moments, including nonlinear effects in VPD that were neglected in previous work.

2. Data

a. Observational data

In our observational analysis, we use daily maximum 2-m air temperature data from the CPC Global Unified Temperature dataset and daily mean surface soil moisture data from

ESA Climate Change Initiative, version 7.1 (ESA-CCI v07.1) (Dorigo et al. 2017; Gruber et al. 2017, 2019). We use summertime (June–August) temperature and soil moisture data from the years 2012 to 2021. Data from the ESA-CCI product represent soil moisture averaged through a 5-cm slab of soil, and only days where no quality control flags were present contributed to the analysis. Though the ESA-CCI data product goes further back than 2012, the data assimilation scheme ingests fewer satellite observations over this period, and the spatial coverage is not as robust, particularly at high latitudes.

b. *Reanalysis product*

We utilize hourly ERA5 reanalysis (Copernicus Climate Change Service 2019) for long-term statistical analyses of soil moisture's influence on temperature extremes and for generating model time series. While observational products could be used for examining the relationship between soil moisture and temperature extremes, we use ERA5 to ensure consistency when we compare ERA5 soil moisture and temperature time series and our model output that is forced by ERA5 shortwave radiation, precipitation, and dewpoint temperature time series. This choice does come with caveats: for example, ERA5 is known to not perfectly conserve water mass (Muñoz-Sabater et al. 2021; Mayer et al. 2021). However, as Benson and Dirmeyer (2021) showed using the Soil Climate Analysis Network (SCAN; Schaefer et al. 2007) and flux network (FLUXNET) observational data (Pastorello et al. 2017), ERA5 reproduces the nonlinear coupling between soil moisture and extreme temperatures well, giving us confidence that ERA5 is fit for the purpose of our study.

Throughout, we use summertime data (June–August) over multiple sites (Southern Great Plains; Wichita, Kansas; Atlanta, Georgia; Dallas, Texas; Washington, D.C.; Minneapolis, Minnesota; and Seattle, Washington) in the range of 1979–2021 at $0.25^\circ \times 0.25^\circ$ resolution. For the majority of our analysis, we use daily mean values for environmental variables; we convert hourly reanalysis output to daily means by averaging over each 24-h period. For our statistical analysis (Fig. 2), we use daily mean 2-m temperature and soil moisture data from the uppermost layer (0–7-cm depth). To generate model time series, we force our dynamical model with daily mean shortwave radiative forcing, precipitation, and dewpoint time series. We compare our model output with daily mean 2-m temperature, soil moisture content (uppermost layer, 0–7 cm), latent heat flux, and the sum of outgoing longwave and sensible heat fluxes in Fig. 4.

3. Evidence from observations and reanalysis

a. *Heat waves and soil moisture in observations*

We begin our analysis by considering observations of soil moisture and extremely high temperatures. We focus on observations because they allow us to demonstrate a widespread relationship between soil moisture and extremely high temperatures without relying on global/regional climate models or reanalysis products. In what follows, we will consider observational data of temperature and soil moisture without removing the seasonal cycle in radiation. This could introduce a third, unaccounted for factor in our analysis below; however, we find that removing the seasonal cycle does not much impact the takeaways of this subsection (see Fig. S1 in the online supplemental material). We will later utilize reanalysis and a dynamical model to perform a more rigorous analysis of this correlation, as the observational record is too short for this purpose.

Observations in Fig. 1a show the connection between extremely hot days and soil moisture deficits in the midlatitudes. A value of 100 in Fig. 1a indicates that all days above the local 99th temperature percentile occurred when the soil was drier than the local 25th percentile (i.e., all points above the orange lines in Figs. 1b–f are also left of the green lines). In many regions, more than 90% of days where temperatures exceed the local 99th percentile occur when the soil is desiccated. The association between low soil moisture and high temperatures is strongest in continental midlatitude regions such as the central United States and central Europe, as well as in subtropical regions with high precipitation variability such as South Asia and the Sahel. The association is weakest in high-latitude regions such as Canada and Siberia and in very arid regions such as the U.S. Southwest and the Sahara. This corroborates model-based explorations of spatially varying land–atmosphere coupling strengths (e.g., Seneviratne et al. 2006a; Santanello et al. 2018).

The difference between areas where the correlation between low soil moisture and high temperatures is sizable and areas where this correlation is moderate to minimal can be visualized in temperature–soil moisture phase space (Figs. 1b–f). In some regions, extremely high temperatures are clustered around periods where the soil is dry. This is consistent with past studies on nonlinearities in the soil moisture–temperature relationship found in observations (Benson and Dirmeyer 2021). Conversely, where soil moisture seems to matter little for temperature extremes, the phase–space relationship between temperature and soil moisture is either (i) relatively flat (like in the Canadian boreal forests shown in Fig. 1c) or (ii) there is too little variability in soil moisture for soil moisture to influence temperatures significantly (like the Arabian Desert shown in Fig. 1d). Explaining this emergent, potentially nonlinear relationship between soil moisture and temperature, or the lack of such a relationship in some regions, is the primary goal of this paper.

b. *Soil moisture and temperature in reanalysis*

To further explore the relationship between temperature and soil moisture and build toward a conceptual, physical understanding of this relationship, we focus on three places in the United States with a range of relationships between soil moisture and near-surface temperature. We use the summertime [June–August (JJA)] ERA5 daily mean temperature and (top-layer) soil moisture data (Copernicus Climate Change Service 2019) for the Southern Great Plains (SGP; we use the Department of Energy Atmospheric Radiation Measurement site for the precise coordinates in this analysis); Atlanta, Georgia; and Washington, D.C. in what follows. Note that the findings below do not depend on whether one considers daily mean or daily maximum temperatures or if

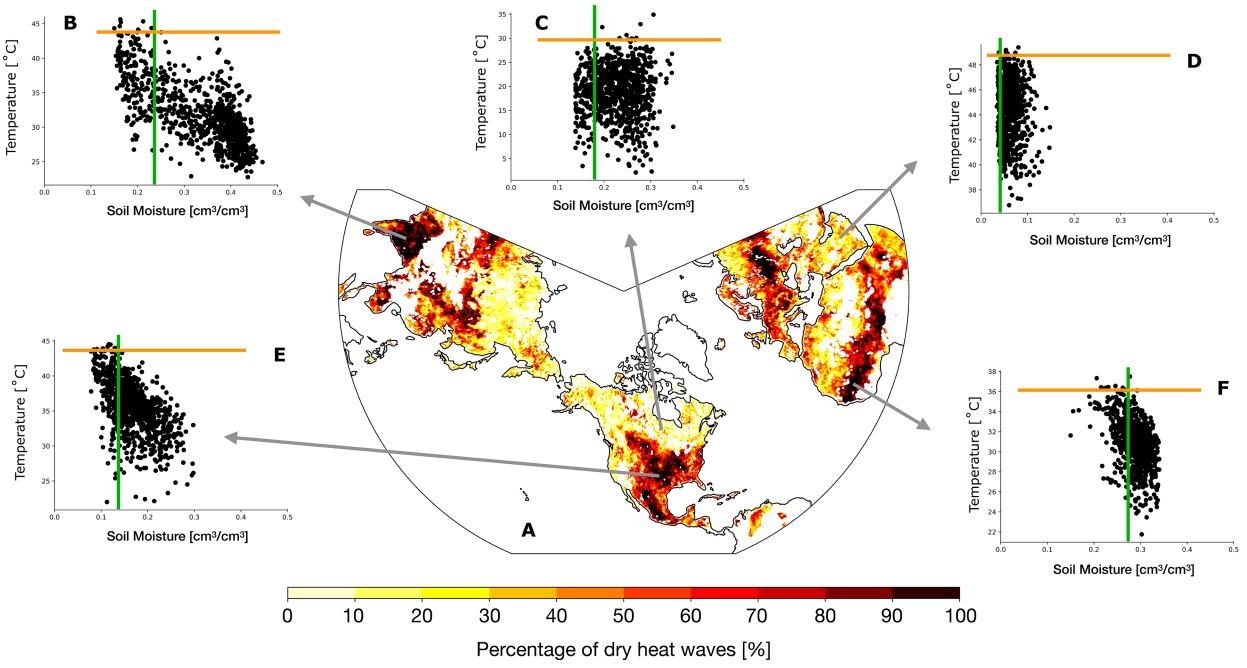

FIG. 1. (a) The percentage of days where the maximum temperature exceeds the local 99th percentile while soil moisture is less than the local 25th percentile. (b)–(f) Daily maximum temperature–soil moisture phase space plots with the horizontal orange line indicating the local 99th temperature percentile and the vertical green line indicating the local 25th percentile for soil moisture. Each panel uses summertime (JJA) daily maximum temperature data from the CPC Global Unified Temperature dataset and daily soil moisture data from the ESA-CCI v07.1 dataset, both over the timespan of 2012–21.

temperatures are viewed as anomalies relative to long-term averages (see Figs. S2 and S3).

In Figs. 2a–c, we show temperature–soil moisture phase space plots that are empirically similar to the plots from Figs. 1b–f from different locations across the globe. The gold lines show the mean temperature after we bin the temperature data by each soil moisture decile and compute the mean. In areas of strong soil moisture influence like the SGP, the mean temperature increases nonlinearly as the soil dries, whereas this phase space is relatively flat in regions of weak coupling (i.e., Washington, D.C.). These locations serve as analogs to the different coupling regimes seen in observations (Fig. 1b for SGP and Fig. 1c for Washington, D.C.).

Though soil moisture variations are associated with ~5°–10°C changes in decile-mean temperatures at each site, we analyze in Figs. 2a–c that the influence of soil moisture on daily temperature variance within each decile is not obvious. We compute probability distribution functions (PDFs) for near-surface temperature after binning by each soil moisture decile (as done in Figs. 2a–c) in Figs. 2d–f and remove the mean temperature from the PDFs in Figs. 2g–i. We find that the PDFs are roughly centered on the origin when the mean temperature is removed, suggesting that soil moisture modifies the mean temperature state but plays less of a role in determining the daily variance for a given level of soil moisture. Figures 2j–l show this more clearly: the standard deviation of temperature is roughly constant across soil moisture levels regardless of the degree to which average temperature is influenced by soil moisture. Indeed, there is no clear pattern of the relationship between temperature variability and soil moisture content that appears across all sites, suggesting that the differences across soil moisture deciles could result from chaotic atmospheric variability.

Based on our analysis in Figs. 1 and 2, we highlight two conclusions that inform our theoretical model. The first is that, while soil moisture seems to play a potentially significant role in modulating the mean state of temperature, it appears to play a lesser role in determining daily temperature variability. The second is that the degree to which soil moisture impacts heat wave frequency and intensity is related to the strength of the nonlinear correspondence between soil moisture and temperature. Indeed, soil moisture has a sizable impact in the SGP which has a strongly nonlinear relationship between soil moisture and temperature, whereas soil moisture has a minimal impact in Washington, D.C., which has a weak nonlinearity strength (see the gold lines in Figs. 2a–c). Atlanta serves as a "middle of the road" example between the SGP and Washington, D.C.

4. Theory for coupling between soil moisture and temperature

Before analyzing the case studies mentioned above, we first present a general theoretical framework that explains how a nonlinear relationship can arise out of the surface energy balance (as was observed in the SGP). Our goal here is not to describe a given location or climate in particular but to remain as general as possible to build intuition for our case studies later.

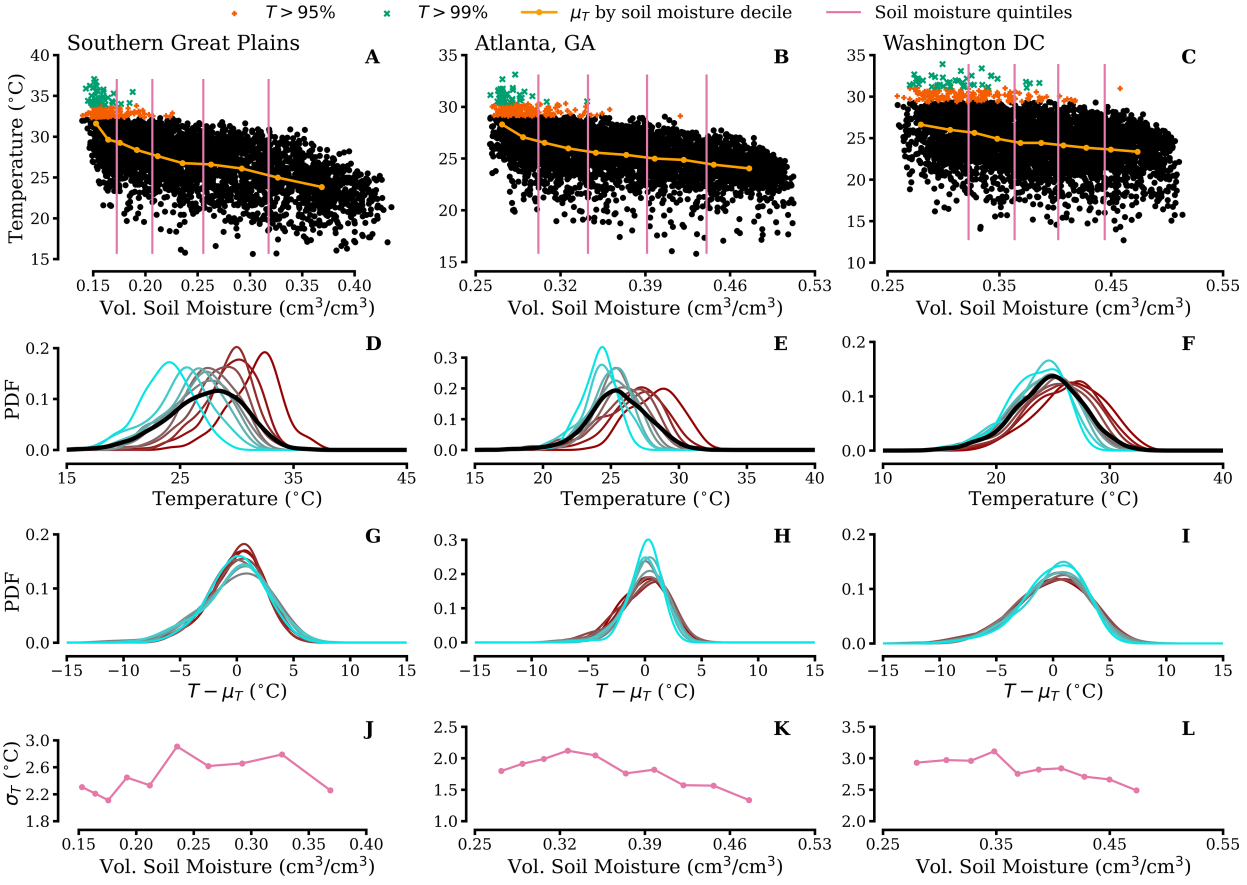

FIG. 2. (a)–(c) Scatterplots of the temperature–soil moisture phase space for three locations, with extreme temperature days colored orange ($T >$ 95th percentile) and green ($T >$ 99th), as well as the mean temperature averaged within each soil moisture decile (gold curve), see the legend above (a)–(c). (d)–(f) The estimated PDF of near-surface temperature conditional on each decile of soil moisture using ERA5 reanalysis output. The cyan (maroon) PDFs are for the high (low) deciles of soil moisture. The mean PDF is in black. (g)–(i) As in (d)–(f), but after subtracting the mean temperature of each PDF. (j)–(l) The standard deviation of the temperature PDF after binning by each soil moisture decile. Each panel uses summertime (JJA) daily average 2-m temperature and daily average soil moisture (of the topmost layer) values from the ERA5 reanalysis product from 1979 to 2021.

First, consider a surface layer with a heat capacity C, temperature T, and volumetric soil moisture content θ. As we are only interested in the influence of soil moisture on energy fluxes, our θ is the quantity of soil moisture available for evapotranspiration, meaning θ is always greater than or equal to the wilting soil moisture threshold (Koster et al. 2004). Energy enters the system via net downward radiation $\mathcal{F}$ and exits the system via the combination of thermal radiation and sensible heat flux that we write as $\mathcal{H}(T)$ and latent heat that we denote as $\lambda\mathcal{E}(\theta, T)$, where λ is the latent enthalpy of vaporization and $\mathcal{E}$ is the evapotranspiration. We assume that ground heat fluxes to lower layers of soil moisture are negligible. We assume that the "dry heat fluxes" (thermal radiation and sensible heat flux) emitted by the surface are purely a function of temperature and the latent heat is a function of both soil moisture content and temperature (Seneviratne et al. 2010). With these definitions, energy conservation implies

$$C\frac{dT}{dt} = \mathcal{F} - \mathcal{H}(T) - \lambda\mathcal{E}(\theta, T). \tag{1}$$

We now make two natural assumptions about the outgoing heat fluxes. The first is that the evapotranspiration is, to first order, the product of two separable functions of temperature and soil moisture content, such that $\lambda\mathcal{E}(\theta, T) = \lambda\ell_\theta(\theta)\ell_T(T)$. Note ℓ_θ and ℓ_T are increasing functions of soil moisture and temperature, respectively, consistent with theory (Budyko 1961) and a number of modeling studies (e.g., Manabe 1969; Sellers et al. 1986; Best et al. 2011; Duan et al. 2024).

The second assumption is that, to leading order, the sum of the dry heat fluxes $\mathcal{H}(T)$ scales similarly to the thermal dependence of the outgoing latent heat flux, such that $\mathcal{H}(T) \approx \alpha\ell_T(T)$, where $\alpha > 0$ determines the strength of the dry fluxes relative to the latent heat flux. This relationship is motivated by the fact that both the dry and latent heat fluxes are increasing functions of temperature and thus, to first order, will possess analogous scalings with temperature, albeit with different sensitivities (hence our inclusion of α above).

Introducing both assumptions outlined above into our (1), we have

$$C\frac{dT}{dt} = \mathcal{F} - [\alpha + \lambda\ell_\theta(\theta)]\ell_T(T). \tag{2}$$

Assuming that the energy fluxes are in equilibrium, we can isolate the temperature dependence of the fluxes, such that

$$\ell_T(T) = \frac{\mathcal{F}}{\alpha + \lambda\ell_\theta(\theta)}. \tag{3}$$

Equation (3) shows that the temperature dependence of surface energy fluxes is nonlinearly related to the soil moisture dependence of the latent heat flux. If we now Taylor expand $\ell_T(T)$ and neglect nonlinear terms such that $\ell_T(T) \approx \ell_T(T_0) + \zeta(T - T_0) + \mathcal{O}(T_0^2)$, where $T_0 > 0$ is an arbitrary reference temperature and $\zeta > 0$, we obtain

$$T(\theta) = \frac{\mathcal{F}}{\zeta[\alpha + \lambda\ell_\theta(\theta)]} + \Gamma(T_0), \tag{4}$$

where $\Gamma(T_0) = T_0 - \ell_T(T_0)/\zeta$ is a function of the reference temperature only (and is therefore constant). Equation (4) implies that a nonlinear relationship between soil moisture and surface temperatures is a generic result of surface energy balance, independent of a given parameterization of the soil moisture–dependent component of the latent heat flux, subject to our assumptions made about the outgoing fluxes.

We can illustrate how different parameterizations of $\ell_\theta(\theta)$ influence the qualitative relationship found in (4). To do so, we normalize all coefficients in (4) and allow $\ell_\theta(\theta)$ to take on a variety of functional forms, with the only restriction being that $\ell_\theta(\theta)$ is sublinear in θ owing to the concave relationship between soil moisture and evapotranspiration that is a consistent feature of land surface models (Budyko 1961; Trugman et al. 2018). Note that in our results, the "piecewise" parameterization refers to a conventional linkage of soil moisture to evapotranspiration designed to distinguish between moisture and energetic limitations on evapotranspiration, where

$$\ell_\theta(\theta) = \begin{cases} \theta, & \theta \le \theta^* \\ \theta^*, & \theta > \theta^* \end{cases}, \tag{5}$$

where $\theta^* > 0$ is a constant and is referred to as the "critical soil moisture value" where evapotranspiration switches from being in a "water-limited regime" (when $\theta < \theta^*$) to being in an "energy-limited regime" (when $\theta > \theta^*$). This parameterization is commonly invoked to explain emergent phenomena in numerical land–atmospheric models (Koster et al. 2004; Hsu and Dirmeyer 2023), though observing the critical value has been challenging (Koster et al. 2006) and the emergent "regimes" have been shown to smoothly transition between one another in process-based land–atmosphere thermodynamic analyses (Vargas Zeppetello et al. 2019). We also include for comparison a "breakpoint" curve to show that our results are consistent with the breakpoint representation of the temperature–soil moisture phase space, as proposed in Benson and Dirmeyer (2021).

Figure 3 shows how temperature relates to soil moisture for various parameterizations of the latent heat flux dependence on soil moisture. The nonlinear coupling between temperature and soil moisture is insensitive to the specification of how the latent heat flux depends on soil moisture. Moreover, we find the presence of two clear regimes: one regime where soil moisture only weakly affects temperature (for high soil moisture values) and one regime where soil moisture strongly influences temperatures (for low soil moisture content). This explains the breakpoints in the temperature–soil moisture phase space found by Benson and Dirmeyer (2021); only our approach has the advantage of smoothly transitioning between each regime. The only assumptions required for this to hold in (4) is that evapotranspiration increases with soil moisture content and that the dry heat fluxes scale, to first order, linearly with temperature. These assumptions are supported by a wide body of literature (Budyko 1961; Seneviratne et al. 2010; Vargas Zeppetello et al. 2022).

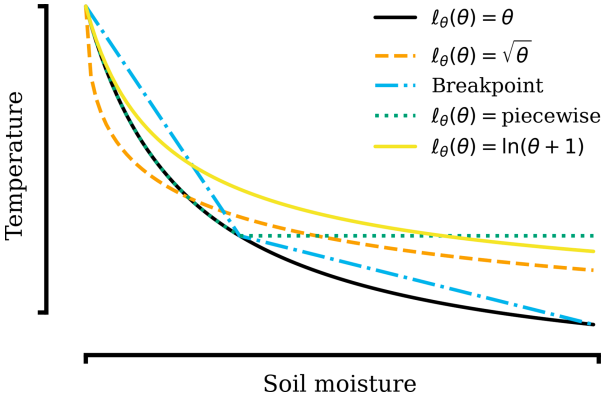

FIG. 3. The influence of different parameterizations for $\ell_\theta(\theta)$ on near-surface temperature using (4) after normalization. Piecewise refers to invoking (5) for $\ell_\theta(\theta)$. The breakpoint curve highlights how a breakpoint model for the temperature–soil moisture phase–space relationship [*à la* Benson and Dirmeyer (2021)] compares with our nonlinear curves (i.e., the black, orange, green, and yellow curves).

5. The soil moisture–atmosphere coupled model

We now turn to a quantitative analysis to quantify the influence of this nonlinearity on temperature extremes. To do so, we build a conceptual soil moisture–atmosphere coupled model (SMACM) based off the framework outlined in section 4. When introducing our parameterizations of the fluxes, we closely follow the procedure outlined in Vargas Zeppetello et al. (2022), see their section 2b.

a. Model formulation

1) PRELIMINARIES

SMACM is a one-dimensional box model of surface temperature and soil moisture, where the land surface is forced by variations in net shortwave radiation and dewpoint temperature. The land surface is described by a dynamic temperature T and soil moisture content m, where m is a value between zero and unity that denotes the fractional saturation of the land

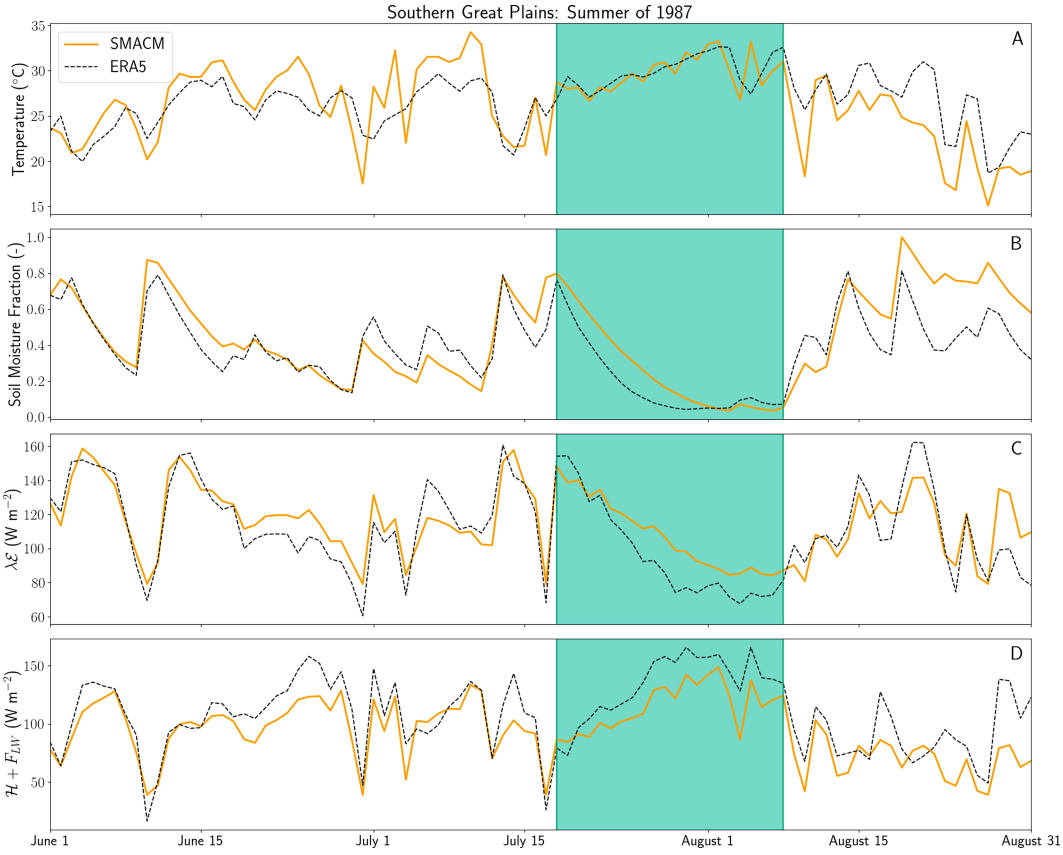

FIG. 4. The (a) 2-m air temperature, (b) soil moisture fraction, (c) latent heat flux, and (d) dry heat flux for the SGP summer of 1987. ERA5 time series are the black dashed lines, while SMACM outputs are the solid gold lines. Each panel uses summertime (JJA) daily average values from the ERA5 reanalysis product from the summer of 1987.

surface. Note here that m refers to the uppermost layer of the soil column. The surface has a heat capacity, C, and analogously, a soil moisture holding capacity is given by $\mu = \rho_l h \theta_{\max}$, where h is the height of the soil column, ρ_l is the density of liquid water, and $\theta_{\max}$ is the maximum available pore space in the soil column that can be occupied by liquid water. The land surface is coupled to a nondynamic atmosphere with dewpoint temperature T_d and reference specific humidity q_r; we will discuss the rationale behind considering these attributes in our modeling framework below.

2) MOISTURE SECTOR

We begin by focusing on the surface water budget. Conservation of water mass at the surface can be written as

$$\mu \frac{dm}{dt} = \mathcal{P} - \mathcal{E} - \mathcal{R} - \mathcal{I}, \tag{6}$$

where $\mathcal{P}$ is precipitation forcing, $\mathcal{R}$ is runoff, and $\mathcal{I}$ is infiltration. All terms in (6) are given in kilograms per square meter per second. Runoff and infiltration are considered to act on far shorter or longer, respectively, time scales than is relevant for our analysis. Hence, runoff and infiltration act to keep soil moisture within restricted bounds set by the field capacity, μ; therefore, $\mathcal{R} = \mathcal{I} = 0$, and we restrict $0 \leq m \leq 1$. Therefore, we have

$$\mu \frac{dm}{dt} = \mathcal{P} - \mathcal{E}. \tag{7}$$

Following previous work (e.g., Manabe 1969; Vargas Zeppetello et al. 2022), the total evapotranspiration from the surface soil layer can be written as

$$\mathcal{E} = \nu m [q_s(T) - q_r], \tag{8}$$

where $q_s(T)$ is the saturation humidity given by the Clausius–Clapeyron relationship and ν is the surface evaporative conductance. In (8), ν captures the influence of vegetation on evapotranspiration, where higher (lower) values of ν represent a land surface that evaporates more (less) liquid water for a given atmospheric demand for water vapor. To simplify (8), we linearize around the dewpoint temperature:

$$\mathcal{E} \approx \nu \gamma m (T - T_d), \tag{9}$$

where γ is the temperature derivative of the Clausius–Clapeyron relationship evaluated at the dewpoint temperature, and we have used the identity $q_s(T = T_d) = q_r$. Using (9) in (6) results in

$$\mu \frac{dm}{dt} = \mathcal{P} - \nu\gamma m(T - T_d). \tag{10}$$

Note that we here neglect the evapotranspiration from deeper soil moisture layers, as this expression is focused only on surface soil moisture content m. By Taylor expanding the evapotranspiration around the dewpoint temperature, we have also not allowed the condensation of dew at the surface, which makes up a negligible fraction of the surface moisture budget during summer.

3) Energy sector

The land surface is forced by net shortwave radiation, denoted as $\mathcal{F}_{\mathrm{SW}}$, that is assumed to be independent of the model state (i.e., we do not account for land–atmosphere feedbacks on shortwave radiation). The energy budget is balanced by latent, sensible, ground, and net longwave channels, denoted by $\mathcal{L}$, $\mathcal{H}$, G, and F_{LW}, respectively. Energy conservation at the surface is written as

$$C\frac{dT}{dt} = \mathcal{F}_{\mathrm{SW}} - F_{\mathrm{LW}} - G - \mathcal{H} - \mathcal{L}, \tag{11}$$

where all terms are given in watts per square metre. Consistent with our linearized parameterization of evapotranspiration given by (9) and following previous work (Vargas Zeppetello et al. 2022), we parameterize the sum of the longwave and sensible heat fluxes as linear departures from the atmospheric dewpoint, such that

$$\mathcal{H} + F_{\mathrm{LW}} \approx \alpha(T - T_d), \tag{12}$$

where $\alpha > 0$ is the dry feedback sensitivity parameter. We approximate the ground heat flux as a constant fraction of the average incoming radiation, $G = \zeta\overline{\mathcal{F}_{\mathrm{SW}}}$, following Martens et al. (2020), where ζ parameterizes the type of vegetation in the area (tall vegetation leads to lower values of ζ and vice versa for shorter vegetation).

We reemphasize that, in our formulation, the dewpoint effectively acts as a reference temperature that the model would relax to on slow time scales if net solar radiation was zero. The motivation for this choice is to maintain a tractable model that also closes the surface moisture budget (Note the energy flux associated with dew condensation in the summertime is negligible in most midlatitude climates, meaning both the moisture and energy budget are approximately closed using this parameterization).

The total evapotranspiration is given by (8), which allows us to write the latent heat flux as

$$\mathcal{L} = \lambda\nu\gamma m(T - T_d). \tag{13}$$

We can now use (12) and (13) in (11) to arrive at

$$C\frac{dT}{dt} = F - (\alpha + \lambda\gamma\nu m)(T - T_d), \tag{14}$$

where we have defined $F := \mathcal{F}_{\mathrm{SW}} - \zeta\overline{\mathcal{F}_{\mathrm{SW}}}$.

4) The soil moisture–atmosphere coupled model

Taking (14) and (10) together, the governing equations of SMACM are given by

$$C\frac{dT}{dt} = F - (\alpha + \lambda\gamma\nu m)(T - T_d), \tag{15}$$

$$\mu \frac{dm}{dt} = \mathcal{P} - \nu\gamma m(T - T_d). \tag{16}$$

For a summary of model parameters and average orders of magnitude used throughout this paper, see Table 1. SMACM can be seen as a linearized version of the soil energy balance model developed by Vargas Zeppetello et al. (2022), see their Eqs. (7) and (8).

b. *SMACM in thermal equilibrium*

Our analysis of the soil moisture–temperature phase space in Fig. 2 (specifically Figs. 2g–l) suggested that soil moisture is associated with 5°–10°C changes in the mean state of temperature but plays less of a role in determining temperature variability. This implies that the time scales over which soil moisture influences temperature are smaller than the time scales over which atmospheric variability influences temperature. Conceptually, this picture aligns with the current understanding of extreme events, which can be thought of as an interaction of different physical mechanisms that possess different characteristic response time scales (Proistosescu et al. 2016).

In appendix A, we make this notion concrete by proving that the time scale associated with purely surface temperature fluctuations [Eq. (15)] is subdaily and is much smaller than that of soil moisture dry-down [Eq. (16)], therefore formalizing a common assumption in various studies (e.g., Koster and Suarez 2001; Seneviratne et al. 2006b). In the parlance of dynamics, this would suggest that SMACM is "time scale separated," wherein one quantity (temperature) varies much faster than another (soil moisture). Since temperature is the fast variable in SMACM, restricting our analysis to slow time scales is equivalent to analyzing the behavior of SMACM in thermal equilibrium.

Before we can invoke thermal equilibrium, we must first check that our parameterizations hold on daily time scales. We first test the validity of our dry heat flux parameterization given by (12) on daily time scales by computing the correlation between average dry heat fluxes ($F_{\mathrm{LW}} + \mathcal{H}$) and the average near-surface temperature anomaly above the dewpoint temperature using a number of averaging windows in ERA5, see Table 2. We find that, the larger the averaging window we consider, the higher the correlation between the two quantities we obtain in a variety of locations. This gives us confidence that our parameterization is fit for purpose on model-relevant time scales.

Second, we must confirm that 2-m dewpoint temperature can be reasonably approximated as an exogenous forcing on 2-m air temperature on daily time scales. This allows us to ignore any influence that 2-m air temperatures may have on 2-m dewpoint temperatures. We verify this assumption by

TABLE 1. List of SMACM state variables, model forcings, physical constants, and parameter names, their symbols, average OM, and units.

	Symbol	OM	Units
State variable			
Surface temperature	T	10^2	K
Time	t	1	s
Soil moisture fraction	m	10^{-1}	—
Model forcing			
Shortwave radiative forcing	$\mathcal{F}_{SW}$	10^2	W m^{-2}
Precipitation	$\mathcal{P}$	10^{-1}	kg H_2O m^{-2} s^{-1}
2-m dewpoint temperature	T_d	10^2	K
Physical constant			
Latent heat of vaporization	λ	2.5×10^6	J kg H_2O^{-1}
Clausius–Clapeyron derivative at mean T_d	γ	10^{-4}	K^{-1}
Effective heat capacity of surface layer	C	10	J K^{-1} m^{-2}
Parameter			
Dry feedback strength	α	10	W m^{-2} K^{-1}
Surface evaporative conductance	υ	10^{-2}	kg H_2O m^{-2} s^{-1}
Soil holding capacity	μ	10	kg H_2O m^{-2}
Dry heat flux offset	ϕ_D	10	W m^{-2}
Latent heat flux offset	ϕ_L	10	W m^{-2}
Ground heat flux fraction	ζ	10^{-1}	—
Maximum fraction of available pore space	θ_{max}	10^{-1}	—

computing the lagged correlation between the two quantities in ERA5 (see Figs. S4–S6). We find negligible correlation between dewpoint temperature and air temperature response on time scales of more than ~3 days, giving us confidence that, on long time scales, dewpoint can be treated as approximately independent from surface temperature. Note that this choice is also consistent with past modeling studies (Vargas Zeppetello et al. 2022).

We can now take advantage of time-scale separation in SMACM to derive two novel theoretical results. The first is a diagnostic relationship between temperature and soil moisture on time scales longer than 1 day. Time-scale separation implies that, on long time scales, the temperature derivative in (15) can be set to zero. This is a common approach in other models that possess more than one characteristic response time scale (e.g., Held et al. 2010). Here, as the time scale we are interested in is supradaily, we set all model forcings to their daily mean values (this applies to $\mathcal{F}_{SW}$, T_d, and $\mathcal{P}$).

TABLE 2. Coefficient of determination (r^2) values in each location between $F_{LW} + \mathcal{H}$ and $T - T_d$ over a number of averaging windows. Note the averaging windows are all in days, i.e., an averaging window of 3 is the regression between the 3-day average sum of dry fluxes and the 3-day average difference in temperature and dewpoint temperature. All results are calculated using the ERA5 reanalysis.

Location	1	3	5	7	14
SGP	0.5487	0.6544	0.6993	0.7236	0.7553
Wichita, Kansas	0.5046	0.6287	0.6837	0.7138	0.7600
Atlanta, Georgia	0.8309	0.8850	0.9035	0.9139	0.9308
Dallas, Texas	0.7618	0.8267	0.8550	0.8708	0.8940
Washington, D.C.	0.7792	0.8437	0.8664	0.8802	0.9048
Minneapolis, Minnesota	0.6435	0.7208	0.7530	0.7745	0.8142
Seattle, Washington	0.6947	0.7887	0.8250	0.8441	0.8718

Solving the SMACM model equations under these assumptions leads to

$$T(m) = T_0\left(\frac{1}{1 + \eta m}\right) + \overline{T}_d, \tag{17}$$

where we have defined a "dry-out temperature"

$$T_0 := \frac{\overline{F}}{\alpha} \tag{18}$$

and a coupling parameter

$$\eta := \frac{\lambda\gamma\upsilon}{\alpha}, \tag{19}$$

where $\overline{F}$ and $\overline{T}_d$ are the daily mean net downward radiative flux and daily mean dewpoint temperature, respectively.

The T_0 and η have salient physical interpretations. The T_0 is the maximum soil moisture–induced temperature departure from the dewpoint temperature (occurring when the surface is completely dry). This upper bound is set purely by the ratio of shortwave forcing to the dry surface response parameter, α. We refer to T_0 as the dry-out temperature for the remainder of this manuscript.

The coupling parameter, η, measures the coupling strength between surface soil moisture and temperature. The strength of the coupling parameter is determined by the relative strength of the latent heat feedback associated with a saturated surface layer to the strength of the dry feedback. This parameter captures the influence of evapotranspiration from surface-level soil moisture on the overall energy budget and conceptually equivalent to the inverse of the Bowen ratio.

In (17), the dewpoint temperature is a background state that is supplemented by the temperature variations attributable to soil moisture. In the language of dynamical systems,

(17) is referred to as a *nullcline*, defined as a manifold in phase space where the dynamics of one or more variables is neglected (Strogatz 2018). Such expressions are useful for the analysis of dynamical systems possessing more than one distinct time scale (e.g., Bauer and Carter 2021). We will henceforth refer to (17) as the temperature nullcline or just "the nullcline" in the remaining discussion.

The second key result is a nonlinear Hasselmann-like model (Hasselmann 1976) for the temperature-driven soil moisture response to stochastic precipitation forcing. Using the nullcline [(17)] for temperature in (16), we can write

$$\mu\frac{dm}{dt} = \mathcal{P} - \nu\gamma T_0\left(\frac{m}{1+\eta m}\right). \tag{20}$$

We see that η again determines the degree of nonlinearity, this time of the response of soil moisture to precipitation forcing. This procedure has decoupled the evolution of temperature and soil moisture on supradaily time scales. Equation (20) has the advantage of allowing us to simulate soil moisture time series under the influence of just two daily mean forcings (downward shortwave and precipitation) with each parameter fit directly to ERA5 reanalysis. Furthermore, (20) admits an analytical solution for its response to precipitation forcing, and we will utilize this analytic solution later to derive the central moments of the soil moisture distribution in terms of model parameters.

c. *Model evaluation*

1) Fitting model parameters

To compute model parameters, we carry out regressions using (12) and (9) on 3-day average fluxes against 3-day average state variable anomalies, where anomalies are computed relative to the climatic mean state, using ERA5 reanalysis over the period 1979–2021 in the months of JJA. The regression of dry fluxes against temperature anomalies relative to the dewpoint results in α, while the regression of evapotranspiration against temperature anomalies relative to the dewpoint (weighted by soil moisture content) results in ν. The remaining free parameters ($\theta_{\max}$ and ζ) were tuned such that we minimize the residuals for the soil moisture and temperature time series, which determines μ and F.

2) Linking surface temperature to 2-m air temperature in ERA5

In performing the prescription described above, we encounter two offset terms, ϕ_D for the dry heat fluxes and $\phi_L := \lambda\phi_E$ for the latent heat flux resulting from additional evapotranspiration ϕ_E, that are given by the intercepts of our regressions. These offsets represent additional heat fluxes, treated as constant in time, that come from land–atmosphere interactions not captured in our model that influence 2-m air temperature and the surface heat fluxes. As an example, the additional dry heat flux could come from net warm air advection, while the additional latent heat flux could come from transpiration of root-level soil moisture into the surface boundary layer or precipitation that evaporates en route to the surface. As we will see, treating these additional fluxes as constant in time is sufficient for reproducing 2-m air temperatures in ERA5. Furthermore, the inclusion of these offsets does not change any of the theoretical results of the paper; they simply change the zero points of 2-m air temperature and the surface fluxes.

We treat the influence of these fluxes on surface temperature the same way that we treated shortwave forcing, with their impact being modulated by surface soil moisture via a nullcline equation. This follows from treating these constant radiative fluxes the same way we treated the ground heat flux, itself a constant heat flux, in the derivation above. Therefore, if we define the adjusted forcing as $F_{\text{adj}} := \mathcal{F}_{\text{SW}} - \phi_D - \lambda\phi_E - \zeta\overline{\mathcal{F}_{\text{SW}}}$, we can compare 2-m air temperature, dry heat fluxes, and latent heat flux in our model (given by $\hat{T}_{2m}$, $\hat{\mathcal{H}}$, and $\hat{\mathcal{L}}$, respectively) against that of ERA5 using the following mappings:

$$\hat{T}_{2m}(m) = F_{\text{adj}}\left(\frac{1}{\alpha+\lambda\gamma\nu m}\right) + \overline{T}_d, \tag{21}$$

$$\hat{\mathcal{H}}(m) = F_{\text{adj}}\left(\frac{\alpha}{\alpha+\lambda\gamma\nu m}\right) + \phi_D, \tag{22}$$

$$\hat{\mathcal{L}}(m) = F_{\text{adj}}\left(\frac{\lambda\gamma\nu m}{\alpha+\lambda\gamma\nu m}\right) + \phi_L, \tag{23}$$

where (22) and (23) were found by using (17) in (13) and (12), respectively.

3) Evaluating model fit

Using the model parameters found via our regression-based procedure described above and daily mean JJA reanalysis shortwave radiation, precipitation, and 2-m dewpoint temperature output from ERA5 1979 to 2021, we integrate (20) and use the resulting soil moisture time series to diagnose temperature and heat fluxes using (21)–(23) over the SGP. The resulting time series are shown in Fig. 4, where we show both ERA5 and SMACM time series in the SGP for the summer of 1987. We use the summer of 1987 because of its prolonged period of soil desiccation between the end of July and the beginning of August that shows how our model captures periods of dry soils, which lead to elevated temperatures, higher dry heat fluxes, and less latent heat. We show a longer validation period for SGP, Atlanta, and Washington, D.C. in Figs. S7–S9 to further support our model verification. We are particularly interested in periods where soil moisture is low (green shading in Fig. 4), where a reduction in the latent heat flux (Fig. 4c) is met with an increase in the sensible and longwave heat fluxes (Fig. 4d), as well as an increase in near-surface air temperature (Fig. 4a). Some high-frequency variability in SMACM is missing because we have not included all of the relevant fast fluctuations in atmospheric circulation (i.e., ϕ_D is constant), such as thermal advection. Despite this, SMACM (i) reproduces soil moisture variations in ERA5 as well as (ii) the partitioning of sensible and latent heat. SMACM is also able to reproduce the long time-scale temperature variations, particularly elevated mean temperatures during times of dry soil moisture conditions. Note that the time-scale separation in SMACM

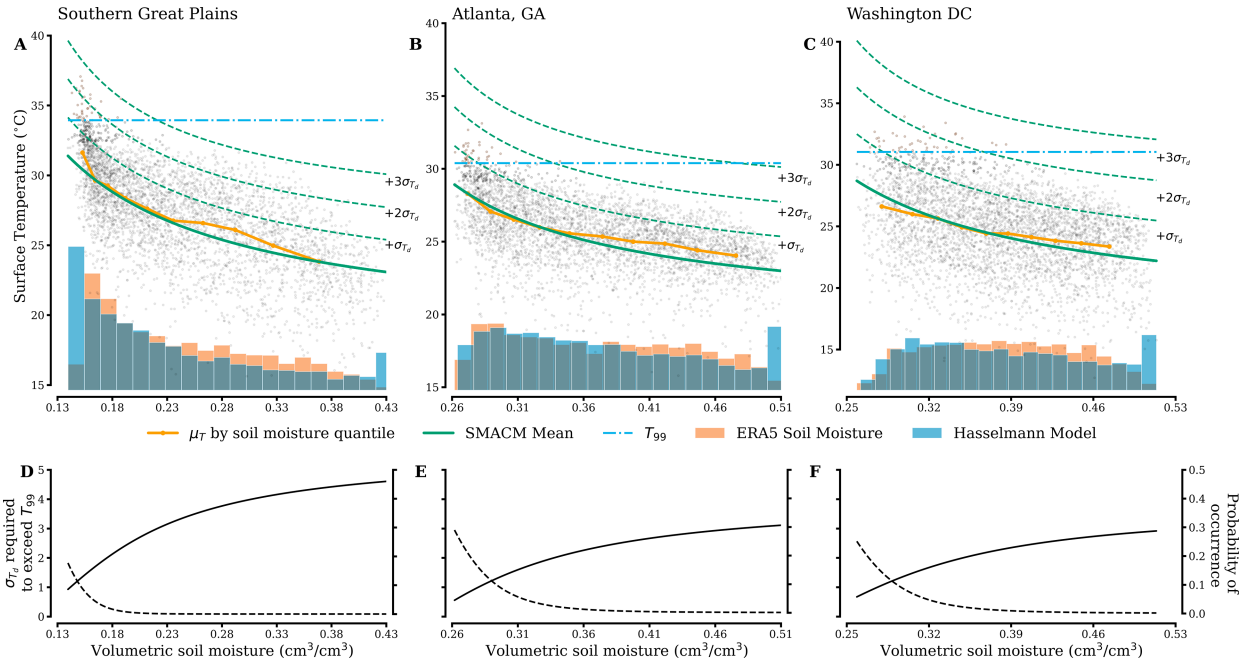

FIG. 5. The temperature–soil moisture phase space for the (a) SGP, (b) Atlanta, and (c) Washington, D.C., with the mean temperature for each soil moisture decile (gold line) and the temperature nullcline [(17), green solid line]. The dashed lines are the nullcline after anomalies of varying size in 2-m dewpoint temperature have been applied. We also show the soil moisture histograms for ERA5 (orange) and our Hasselmann model [(20), light blue]. In (d)–(f), the solid lines show the required anomaly size in the 2-m dewpoint temperature for 2-m temperature given by (17) to exceed the 99th percentile in each location as a function of soil moisture. The dashed lines represent the probability of such an anomaly to occur, assuming a normally distributed dewpoint temperature. (a)–(c) use summertime (JJA) daily average 2-m temperature and daily average soil moisture (of the topmost layer) values from the ERA5 reanalysis product from 1979 to 2021.

described earlier is not clearly observed in Fig. 4 owing to rain that buffets the temperature response.

6. The role of soil moisture in temperature extremes

We can now utilize SMACM to understand how soil moisture influences temperature extremes. One caveat to what follows is that we choose to focus on the same case studies outlined in Fig. 2, as these locations span the range of possible soil moisture–temperature phase spaces (i.e., minimal to strong correspondence), as opposed to analyzing the entire midlatitudes. This approach has the advantage of allowing for more detailed study of representative scenarios but lacks in providing a truly global picture [see Duan et al. (2024) for a global analysis of this topic using fully coupled climate models].

a. Heat wave frequency

The nullcline can be used to understand how soil moisture influences heat wave frequency. In Figs. 5a–c, we show the daily temperature–soil moisture phase space of the SGP, Atlanta, and Washington, D.C. with the temperature nullcline overlaid in green, assuming climatological values (computed using reanalysis) for the net shortwave radiation and dewpoint temperature. We find that the nullcline accurately captures the mean influence of soil moisture on temperature across coupling regimes (i.e., where η is large and small, as is the case in SGP and Washington, D.C., respectively). Moreover, the nullcline also captures the nonlinear influence of soil moisture on temperatures, providing a physical underpinning for the breakpoints observed in the temperature–soil moisture phase space (without invoking a breakpoint in the flux parameterizations) (Benson and Dirmeyer 2021). We apply dewpoint temperature anomalies to the nullcline in each location to show the impact of atmospheric variability on the orientation of the nullcline in phase space (dashed green lines). (An analogous figure for radiative forcing anomalies has identical implications, see Fig. S10.)

When the soil is dry, less extreme dewpoint temperature anomalies are needed to exceed the local 99th temperature percentile than when the soil is wet. We calculate the anomaly size needed to exceed the local 99th percentile, as well as the probability of such an event occurring, as a function of soil moisture in Figs. 5d–f. For the SGP, the anomaly size required grows nonlinearly with soil moisture, whereas in Washington, D.C., the anomaly size is relatively flat. The higher the degree of nonlinearity between temperature and soil moisture (i.e., higher η values), the more the dry soils load the dice in favor of heat waves. The converse is also the case: in regimes where soil moisture is strongly coupled to temperature, wet soils imply that the odds of a heat wave occurring are incredibly small.

TABLE 3. We calculate the ratio of temperature variance owing to soil moisture to total temperature variance for seven locations in the continental United States. We also show the ratio of the dry-out temperature, T_0, to the maximum departure from the mean dewpoint temperature in the reanalysis product, $T_X := \max(T) - \overline{T}_d$, for seven locations in the continental United States. Provided as well are the nonlinear strength parameter η, the dry-out temperature T_0, and the mean and variance of the soil moisture distribution in each location.

Location	η (–)	T_0 (°C)	$\overline{m}$ (–)	σ_m^2 (–)	$\sigma_{T_m}^2/\sigma_T^2$ (–)	T_0/T_X (–)
SGP	1.81	13.0	0.36	0.06	0.42	0.70
Wichita, Kansas	1.80	11.9	0.41	0.07	0.36	0.71
Atlanta, Georgia	1.74	9.31	0.42	0.07	0.49	0.69
Dallas, Texas	1.59	11.2	0.31	0.07	0.55	0.69
Washington, D.C.	1.40	11.15	0.49	0.06	0.22	0.82
Minneapolis, Minnesota	1.08	10.6	0.31	0.04	0.13	0.76
Seattle, Washington	0.61	6.54	0.34	0.05	0.05	0.38

This phenomenon can be explained by the coupling parameter η determining the curvature of the nullcline, i.e., we can write

$$\Delta T := \frac{T(m=1) - T(m=0)}{T_0} = \frac{\eta}{\eta + 1}. \tag{24}$$

If η is small (weak coupling regime), then $\Delta T \sim 0$, and soil moisture's influence on temperature disappears by virtue of the nullcline "flattening out." This would occur in regimes where the dry feedbacks dominate the latent feedbacks. If η is large (strong coupling regime), then $\Delta T \sim 1$, resulting in the maximum difference between temperatures when the soil is dry or wet. Such behavior is concurrent with a "water-limited" coupling of soil moisture and evapotranspiration, and thus, temperature, in a given location.

The nullcline equation clearly quantifies how the nonlinear coupling between soil moisture and temperature influences heat wave frequency: in locations with high η parameters, relatively common atmospheric events can cause temperature extremes when the soil is dry, implying that the frequency at which the soil dries out is a leading order indicator of heat waves in these locations. In locations with low η parameters, soil moisture matters little for heat wave frequency, if at all, owing to its minimal influence on near-surface temperatures.

As a quantitative exercise, we use (17) to compute the ratio of temperature variance owing to soil moisture to total temperature variance in seven locations. We utilize the ERA5 daily mean soil moisture time series at each location and use it to force (17) with the shortwave forcing and the dewpoint temperature set to their climatological average values (to isolate the role of soil moisture). The variance is then taken and compared with the total temperature variance from ERA5 in each location. The parameter values at each location (i.e., η and T_0) are calculated by fitting the model to ERA5 time series, as was done in Fig. 4. Soil moisture mean and variance is calculated from ERA5.

The results of this exercise are shown in Table 3. We find that in locations where η and T_0 are large, and soil moisture is generally dry while still maintaining nonnegligible variance, the ratio of soil moisture–induced daily temperature variance to total daily temperature variance is significant ($\gtrsim$40%). Meanwhile, areas like Washington, D.C., Seattle, and Minneapolis have relatively low η and/or T_0, leading to a small fraction of temperature variance owing to soil moisture. These findings corroborate the results from Fig. 1, where higher fractions of dry heat waves are found where the ratio of temperature variances seen in Table 3 is highest, and the lower fractions are found where variances are lowest.

b. *Heat wave intensity*

Soil moisture's impact on heat wave intensity can be determined by assuming the soil is dry (if the soil is wet, heat waves are either just as or far less likely than when the soil is dry, depending on the coupling strength, see Figs. 5d–f). In this regime, the departure of temperature away from the dewpoint temperature is determined by T_0 or "dry-out" temperature. Atmospheric dynamics impact the nullcline by altering the magnitude of the dry-out temperature. (Recall T_0 linearly depends on $\mathcal{F}_{\text{SW}}$.) Thus, when shortwave forcing is high, the impact of the land thermodynamics on near-surface temperature is exacerbated, particularly when the soil is dry. Our framework therefore suggests an important feedback mechanism between the atmospheric forcing and local thermodynamics, where strong atmospheric forcing makes the land response more skewed toward extremely high temperatures. This finding is congruent with another recent theory of temperature extremes, which posits that soil moisture acts orthogonally to the influence of atmospheric dynamics and controls how close to the theoretical upper bound the land is able to rise to Zhang and Boos (2023). We find that, with the exception of Seattle, T_0 captures at least 65% of the temperature departure from the mean dewpoint temperature on the hottest day in the reanalysis product (see Table 3), despite our omission of any intricacies related to atmospheric forcing (i.e., blocking events) in our framework.

c. *Soil moisture variability*

So far, we have consistently invoked dry soil conditions to demonstrate the role of soil moisture in temperature extremes. But how often does the soil dry out? Indeed, the nonlinearity between temperature and soil moisture described above is a necessary but not sufficient condition for soil moisture dynamics being a leading order factor in heat wave frequency. Soil moisture is impacted by both precipitation frequency and intensity that ultimately control its influence on temperature. For example, if the temperature nullcline is highly nonlinear, but the soil is perpetually dry or wet, then the nonlinearity does not matter because soil moisture is

too restricted in phase space to cause significant temperature variance (the Arabian Desert, shown in Fig. 1d, is an example of this scenario). Hence, the soil moisture distribution also plays a crucial role in assessing the amount of temperature variance owing to soil moisture.

We can utilize (20) to determine the controls on the underlying soil moisture distribution. First, we compute the distribution of soil moisture when (20) is forced with ERA5 precipitation time series in Figs. 5a–c and see that our model largely reproduces the distribution of soil moisture found in ERA5, despite neglecting atmospheric forcing other than precipitation. We can further understand the controls on the soil moisture distribution by solving for its moments analytically. We can carry out this calculation in three parts. First, we solve (20) in the period immediately after a rain event, i.e., when the initial soil moisture content is nonzero and $\mathcal{P} = 0$. We then allow the precipitation to be modeled as a series of instantaneous injections into the soil, and using our solution for when $\mathcal{P} = 0$, we construct the full solution to (20). Last, we solve for the moisture distribution moments using stochastic calculus.

d. *Analytic solution to the nonlinear Hasselmann-like model*

1) SINGLE EVENT

The response of (20) can be analytically solved for in the following way. Consider a completely dry soil column that is injected with moisture owing to a rain event of intensity $0 < p \leq 1$ occurring at $t = t_0$. We assume, for now, that for all times $t > t_0$, no rain occurs. Then, the soil moisture dynamics after the rain event are governed by (20) with $\mathcal{P} = 0$. With this setup, we can investigate the dry-down dynamics by considering

$$\mu \frac{dm}{dt} = -\nu\gamma T_0\left(\frac{m}{1 + \eta m}\right), \tag{25}$$

which can be solved via direct integration. After rearranging and carrying out the integral, we have

$$\ln m(t) + \eta m(t) = \ln p + \eta p - \frac{(t - t_0)}{\tau}, \tag{26}$$

where we have defined

$$\tau := \frac{\mu\lambda}{\eta\overline{F}}. \tag{27}$$

Here, τ is a time scale associated with soil moisture dry-down.[1] Exponentiating each side of (26) and multiplying both sides by η, we have

$$\eta m(t) e^{\eta m(t)} = \eta p e^{\eta p} e^{-(t-t_0)/\tau}, \tag{28}$$

which can be solved for $m(t)$ using the principle branch of the Lambert W function (Corless et al. 1996), such that

$$m(t) = \frac{1}{\eta} W_0(\eta p e^{\eta p} e^{-(t-t_0)/\tau}). \tag{29}$$

Equation (29) tells us that after a rain event, soil moisture decays polylogarithmically toward zero as $t \to \infty$, rather than exponentially, a consequence of considering the full nonlinear dynamics in (20). This dry-down pathway is unique to the literature, as it is often assumed that soil moisture dry-down follows an exponential decay profile (e.g., Teuling et al. 2006; McColl et al. 2019; Vargas Zeppetello et al. 2022).[2] We find that, within our modeling framework, the exponential decay approximation only holds after small rain events, since $m(t) \approx p \exp[-(t - t_0)/\tau]$ for small p, see Fig. 6.

2) FULL SOLUTION

We will now construct the solution to (20) for a series of rain events. Precipitation events, in this model, are instantaneous injections of moisture into the soil column, where the intensity of each event is drawn from a gamma distribution, and events occur in Poisson intervals (Eagleson 1978). Hence, for N rain events, we have

$$\mathcal{P}(t) = \sum_{i=1}^{N} p_i \delta(t - t_i), \tag{30}$$

where p_i is the intensity of each event, t_i is the time at which the event occurs, and $\delta(x)$ is the Kronecker delta function. Given that (29) dictates the remaining moisture at every time t after one precipitation event occurs, for a set of precipitation events with intensity p_i occurring at $t = t_i$, the moisture time series can be written as a sum of each precipitation event's contribution to the soil moisture column, such that

$$m(t) = \frac{1}{\eta} \sum_{i=1}^{N} \theta(t - t_i) W_0[\eta p_i e^{\eta p_i} e^{-(t-t_i)/\tau}], \tag{31}$$

where $\theta(x)$ is the Heaviside function, defined as

$$\theta(x) := \begin{cases} 0 & x < 0, \\ 1 & x \geq 0. \end{cases} \tag{32}$$

An important approximation made in formulating (31) is we assumed that a nonlinear differential equation obeys the superposition principle, which is, in general, not true. However,

[1] Note that τ is not to be interpreted as the "characteristic" time scale of soil moisture dry-down, as a characteristic time scale is canonically defined as a time scale τ such that $m(t) = pe^{-t/\tau}$, which does not accurately capture the behavior of soil moisture in our model, see (29).

[2] Our finding that the soil moisture dry-down profile follows polylogarithmic decay rather than exponential decay is not at odds with such previous work, however, given that each of these papers finds dry-down time scales via fitting an exponential profile to soil moisture dry-down data. Using an exponential decay profile in this application significantly simplifies the task of computing soil moisture dry-down time scales, and, as these authors have shown, captures the relevant processes reasonably well. However, our approach, which is to fit a model to *fluxes* directly and then find the soil moisture dry-down profiles analytically, results in values of the dry-down time scale in terms of flux parameters such as the dry response and surface conductance; this information is not present when fitting directly to data. This explains the insufficiency of using an exponential model in our case, shown in Fig. 6.

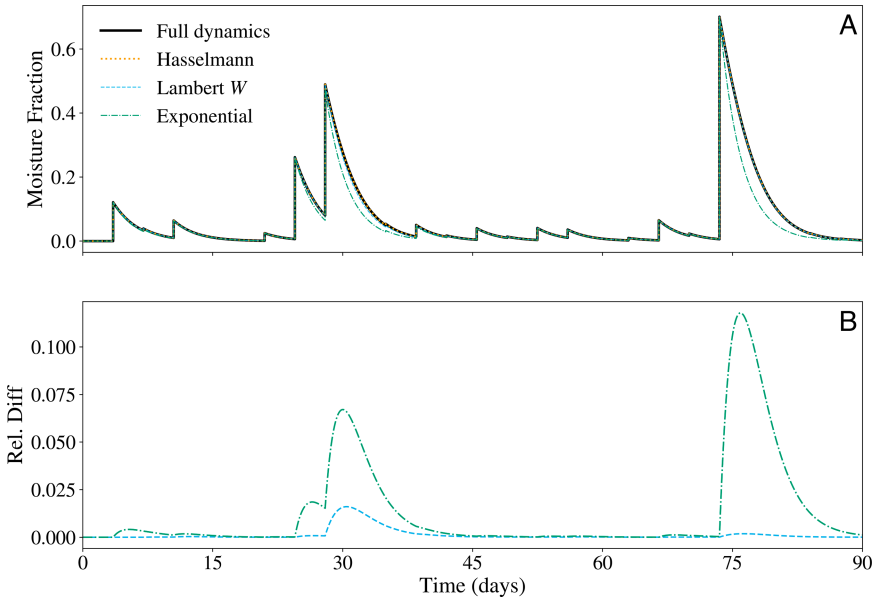

FIG. 6. (a) The soil moisture time series solved for by numerically integrating the full dynamics (15) and (16) (black line). The gold dotted curve shows a numerical integration of (20) and the blue dashed curve show the corresponding (31). The green curve shows the solution to (20) if an exponential decay profile (rather than a Lambert W profile) is assumed. These simulations are over one summer, with synthetic precipitation noise modeled after (30) and parameter values found after fitting the model to ERA5 data. (b) The relative difference between the gold curve and the blue and green curves in the top panel.

numerical simulations show that inaccuracies in (31) occur only after a rain event and decay to the numerical solution in time, see Fig. 6. Hence, we conclude that (31) is a sufficiently accurate approximation of the full dynamics for our purposes.

e. *Solving for the moments of the moisture distribution*

We now solve for the moisture distribution moments by assuming that precipitation can be modeled as individual events whose amplitude is drawn from a gamma distribution and that occur at Poisson intervals (Eagleson 1978). Consider (20) and allow the precipitation to be modeled by (30). This parameterization of precipitation can be referred to as "shot noise" (Rice 1977). For initially dry soil that experiences a precipitation event with intensity p at $t = t_i$, according to (29), the moisture time series is given by (29). With the solution in hand, we can compute the moments of the moisture distribution. Appropriating the setup from Vargas Zeppetello et al. (2022), we compute the noncentral moments of the soil moisture distribution in appendix B [see Eqs. (B14) and (B17)–(B19)], which we use to derive the central moments as

$$\mu_m := \overline{m} = \mathcal{Z}\overline{p} + \frac{\omega\lambda\mu}{2\overline{F}}\overline{p^2}, \tag{33}$$

$$\sigma_m^2 := \overline{m^2} - \mu_m^2 = \frac{\mathcal{Z}}{2}\overline{p^2} + \frac{\omega\lambda\mu}{3\overline{F}}\overline{p^3}, \tag{34}$$

$$\mathcal{S}_m := \frac{\overline{m^3} - 3\mu_m\sigma_m^2 - \mu_m^3}{\sigma_m^3} = \sqrt{\frac{1}{\mathcal{Z}}}\left(\frac{\overline{p^3}}{3} + \frac{\eta\overline{p^4}}{4}\right)\left(\frac{\overline{p^2}}{2} + \frac{\eta\overline{p^3}}{3}\right)^{-3/2}, \tag{35}$$

where $\omega > 0$ is the frequency of rain events, μ_m is the mean, σ_m^2 is the variance, and $\mathcal{S}_m$ is the skewness, and we have defined $\mathcal{Z} := \omega\tau$.

Our results corroborate previous analysis that found the soil moisture distribution was crucially reliant on the ratio of the drying time scale (τ in our framework) and the periodic spacing of precipitation events (given by ω) (Vargas Zeppetello et al. 2022). However, previous work assumed an exponential dry-down profile for soil moisture in response to precipitation events, which we have shown to not be the case in general [see (31)]. This inclusion of a nonlinear response of soil moisture to precipitation events has implications for the moments of the soil moisture distribution: an additional term is included in each central moment that depends on higher moments of the precipitation distribution. Indeed, the nth soil moisture moment depends on the $(n + 1)$th moment of precipitation. This calculation shows how the additional nonlinear effects of soil moisture's response to precipitation forcing influences the resulting moments of the soil moisture distribution, and thus soil moisture's influence on temperature extremes.

7. Synthesis

We have explored the modulation of heat waves by soil moisture found in observations (see Fig. 1) by showing that near-surface temperature fluctuations can be reliably decomposed into a component driven by rapid atmospheric variability and another driven by slow soil moisture dynamics

(see Fig. 2). We find that slow soil moisture variability has a potentially nonlinear impact on the background temperature state, depending on the surface characteristics, while rapid atmospheric variability is well approximated as linearly additive on the top of background state variations (Figs. 2g–l). We then developed a general theoretical framework to understand why this is the case and how a nonlinear relationship between soil moisture and temperature arises out of simple energy and mass balance. We turn this general framework into an empirical model, which encodes the fast and slow modes of temperature variability into a unified, two-time-scale dynamical system. The same nonlinear coupling between soil moisture and temperature that we found in observations and reanalysis is captured by our empirical approach via a coupling parameter, η, that is roughly equivalent to the inverse of the local Bowen ratio. We also find that the slow soil moisture variability is well approximated as primarily driven by stochastic precipitation, with other atmospheric forcing factors likely playing a secondary role (Figs. 5a–c).

Both a strong nonlinear coupling and significant soil moisture variability are required for soil moisture to be a strong control on heat waves. The degree of nonlinearity is encoded in the temperature nullcline [Eq. (17)] via the coupling parameter η, which represents, in our framework, a kind of Bowen ratio. The coupling parameter varies across space and depends on land surface properties (such as the surface conductance). Differences in the strength of the nullcline partially explain the heterogeneity of soil moisture's influence on temperature extremes. In strongly coupled locales (where η is large), moisture depletion increases the potential for a heat wave, and atmospheric anomalies turn this potential into actuality. In weakly coupled locales (where η is small), soil moisture matters little for temperature extremes, as the nullcline "flattens out" and temperature extremes are determined primarily by atmospheric forcing.

By combining the nullcline (17) with the Hasselmann-like model for soil moisture (20), we carry out two calculations. The first quantifies the fraction of temperature variance attributable to soil moisture variability alone. We find that the fraction of temperature variance attributable to soil moisture fluctuations is highest in the same locations where heat waves disproportionately favor dry soils (see Fig. 1). Our analysis would therefore suggest that, over a majority of the continental midlatitudes, heat waves are conditioned on precipitation deficits depleting soil moisture and priming the surface for temperature extremes when a favorable atmospheric anomaly occurs.

The second calculation is a set of analytic expressions for the soil moisture distribution central moments, where we innovate on previous studies by allowing the full nonlinear soil moisture response to be present. We find both similarities and differences with previous analyses. Each soil moisture central moment depends on a key hydrological ratio of time scales: the ratio of the intermittency of rainfall and the time scale of dry-down. However, by including the nonlinear response of soil moisture to precipitation forcing, additional terms are present, which capture the influence of higher precipitation moments on the distribution of soil moisture.

In conclusion, our work presents a conceptual understanding of the role of soil moisture on temperature extremes. Our empirical model reproduces the spatial heterogeneity of soil moisture's influence on temperature variability near the surface, and our Hasselmann-like model for soil moisture variability highlights the key controls on the underlying soil moisture distribution. Moreover, our model explains the arising of breakpoints in the temperature–soil moisture phase space and allows smooth transitions between the two regimes. However, our framework is, by its very design, limited, and further work is needed to unify our model with more complex representations of, say, boundary layer dynamics. Such improvements would enhance the physical picture presented here and allow for a more thorough analysis of the drivers of heat waves to be carried out. Another fruitful direction for future work could be focusing on humid temperature extremes [which are important for extreme, harmful levels of heat stress (Sherwood and Huber 2010)] by possibly using a framework similar to the one used here to understand the nonlinear relationship between soil moisture and wet-bulb temperature found in ERA5 (Kong and Huber 2023).

Acknowledgments. We thank three anonymous reviewers and the editor for helpful comments that improved the manuscript. We also thank Yi Zhang, David Battisti, Karen McKinnon, Peter Huybers, and the Huybers research group at Harvard University for helpful discussions related to this work. A. M. B. is supported by a National Science Foundation Graduate Research Fellowship Grant DGE 21-46756. L. R. V. Z. is supported by the James S. McDonnell Foundation and the Harvard University Center for the Environment. Computations were performed on the Keeling computing cluster, a computing resource operated by the School of Earth, Society and the Environment (SESE) at the University of Illinois Urbana-Champaign.

Data availability statement. All data used in this study are available in public repositories. The code to reproduce our plots is on the corresponding author's GitHub (https://github.com/adam-bauer-34/BVZP-SM-Tex-SMACM-reprod), see released version 1.0.0.

APPENDIX A

Proof of Time-Scale Separation in SMACM

In section 5, we argued that all temperature variability can be decomposed into a "slow" mode driven by soil moisture fluctuations and a "fast" mode driven by fluctuations in shortwave radiation and thermal advection. Here, we prove that, within SMACM, the time scale of thermal adjustment is fast relative to moisture adjustment, thus justifying our separation of time-scale approach.

Assume in all that follows $\mathcal{P} = 0$, as we are analyzing the *response* of SMACM's model equations to precipitation forcing. Thus, the relevant equations are

$$\frac{dT}{dt} = \frac{1}{C}[F - (\alpha + \lambda\gamma\nu m)(T - T_d)] =: f_T(m, T), \tag{A1}$$

$$\frac{dm}{dt} = -\frac{\nu\gamma m(T - T_d)}{\mu} =: f_m(m, T), \tag{A2}$$

where we have defined the right-hand sides of each equation for simplicity in what follows.

a. Step 1: Equilibrium analysis

The equilibria of (A1) and (A2) correspond to the set of solutions of the algebraic system $f_T(m, T) = f_m(m, T) = 0$. The $f_m(m, T) = 0$ implies there are two equilibrium, namely, $m = 0$ and $T = T_d$. However, $T = T_d$ does not satisfy the condition $f_T(m,T = T_d) = 0$ for any m, as $F \neq 0$ by assumption and C is finite. Therefore, the sole equilibrium is given by $(m^*, T^*) = (0, T^*)$, where $T^* := F/\alpha + T_d$. This makes intuitive sense and is supported by other theories of temperature extremes (Zhang and Boos 2023): the only equilibrium is a totally dry soil column, and the temperature is prescribed solely by atmospheric conditions and thermodynamic attributes of the surface.

b. Step 2: Determine stability of equilibrium

The stability of the equilibrium above is determined by the Jacobian of (A1) and (A2) (Strogatz 2018). Therefore, we evaluate

$$\mathcal{J}(m, T) = \begin{bmatrix} \partial_T f_T(m, T) & \partial_m f_T(m, T) \\ \partial_T f_m(m, T) & \partial_m f_m(m, T) \end{bmatrix}, \tag{A3}$$

$$= \begin{bmatrix} -(\alpha + \lambda\nu\gamma m)/C & -\lambda\nu\gamma(T - T_d)/C \\ -\nu\gamma m/\mu & -\nu\gamma(T - T_d)/\mu \end{bmatrix}, \tag{A4}$$

where $\partial_x := \partial/\partial x$. Evaluating (A4) at (m^*, T^*) results in

$$\mathcal{J}(m^*, T^*) = \begin{pmatrix} -\alpha/C & -\lambda\nu\gamma F/C\alpha \\ 0 & -\nu\gamma F/\mu\alpha \end{pmatrix}. \tag{A5}$$

Equation (A5) is an upper triangular matrix, and therefore, the eigenvalues lie on the diagonals, and the corresponding eigenvectors are the columns (Axler 1997). Therefore, the eigenvalues are

$$E_1 := -\frac{\alpha}{C}, E_2 := -\frac{\nu\gamma F}{\mu\alpha}. \tag{A6}$$

As both eigenvalues are negative, the equilibrium (m^*, T^*) is a stable node (Strogatz 2018).

c. Step 3: Solve for eigenvectors

As mentioned above, the eigenvectors are the columns of (A5). Therefore, we have

$$\boldsymbol{\xi}_1 := \begin{pmatrix} 1 \\ 0 \end{pmatrix}, \boldsymbol{\xi}_2 := \begin{pmatrix} \dfrac{F\lambda\nu\gamma\mu}{CF\nu\gamma - \alpha^2\mu} \\ 1 \end{pmatrix}, \tag{A7}$$

where we have simplified each eigenvector to illustrate the point that $\boldsymbol{\xi}_1$ points solely along the T axis and therefore corresponds to thermal adjustments only. It follows that the time scale associated along this direction of decay corresponds to the time scale of thermal adjustment, whereas the time scale of decay along $\boldsymbol{\xi}_2$ corresponds to moisture adjustment (and the resulting temperature adjustment as the soil dries). This proves that temperature has two modes that evolve on different time scales, as represented in (17).

d. Step 4: Compare time scales of decay

The time scales of decay along $\boldsymbol{\xi}_1$ and $\boldsymbol{\xi}_2$ are found by taking the absolute value and inverse of their corresponding eigenvalues (Strogatz 2018), such that

$$\tau_1 = \frac{C}{\alpha}, \quad \tau_2 = \frac{\mu\alpha}{\nu\gamma F}. \tag{A8}$$

Using the average order of magnitude (OM) of each parameter from Table 1, we find that

$$\frac{\tau_2}{\tau_1} \sim 10^6. \tag{A9}$$

Thus, we have shown that the time scale of purely thermal adjustment τ_1 is fast relative to the time scale of moisture adjustment and its influence on temperature τ_2 as desired.

APPENDIX B

Computation of Soil Moisture Distribution Moments

The natural logarithm of the characteristic function $\Psi(\lambda)$ is the Fourier transform of the density function, which for shot noise is given by

$$\ln\Psi(\varrho) = \int_0^\infty f(p')dp' \int_0^\infty \omega\{\exp[i\varrho m(t', p')] - 1\}dt', \tag{B1}$$

such that

$$\Psi(\varrho = 0) = 1, \tag{B2}$$

where ω is the average rainfall frequency and $f(p)$ is the probability density function of the precipitation intensities p_n. Then, the n moments of the moisture distribution are given by the derivatives of the characteristic function, such that

$$\overline{m^n} = -i^n \frac{\partial^n \Psi}{\partial \varrho^n}\bigg|_{\varrho=0}. \tag{B3}$$

We may now introduce the notation

$$\zeta_n := \int_0^\infty f(p')dp' \int_0^\infty m(t', p')^n dt', \tag{B4}$$

which can be solved for in the following way. We use (29) in (B4) to write

$$\zeta_n = \int_0^\infty f(p')dp' \int_0^\infty m(t', p')^n dt'$$
$$= \frac{1}{\eta^n} \int_0^\infty f(p')dp' \int_{t_i}^\infty W_0[\eta p e^{\eta p} e^{-(t'-t_i)/\tau}]^n dt', \quad \text{(B5)}$$

where we have absorbed the Heaviside function by changing the bounds of integration. We perform our first variable substitution as

$$u := \eta p e^{\eta p} e^{-(t-t_i)/\tau}, \quad \text{(B6)}$$

such that

$$du = -\frac{u}{\tau} dt', \quad \text{UB} = 0, \quad \text{LB} = \eta p e^{\eta p}. \quad \text{(B7)}$$

The variable substitution given by (B6) results in the integral

$$\zeta_n = \frac{\tau}{\eta^n} \int_0^\infty f(p')dp' \int_0^{\eta p' e^{\eta p'}} \frac{W_0(u)^n}{u} du, \quad \text{(B8)}$$

where we have absorbed the negative sign by swapping the upper and lower bounds of integration. We now perform a second variable substitution, such that

$$v := W_0(u), \quad \text{(B9)}$$

or, equivalently,

$$u = v e^v \quad \text{(B10)}$$

by the definition of the Lambert W function. Then,

$$du = (v+1)e^v dv, \quad \text{UB} = W_0(\eta p e^{\eta p}) = \eta p, \quad \text{LB} = 0, \quad \text{(A11)}$$

since $W_0(0) = 0$ and $W_0(xe^x) = x$. When (B9) is used in (B8), we are enabled to write

$$\zeta_n = \frac{\tau}{\eta^n} \int_0^\infty f(p')dp' \int_0^{\eta p} (v^n + v^{n-1}) dv, \quad \text{(B12)}$$

which solves exactly to

$$\zeta_n = \frac{\tau}{\eta^n} \int_0^\infty f(p')dp' \left(\frac{\eta^{n+1} p^{n+1}}{n+1} + \frac{\eta^n p^n}{n} \right). \quad \text{(B13)}$$

Carrying out the precipitation integral results in

$$\zeta_n = \frac{\tau \eta}{n+1} \overline{p^{n+1}} + \frac{\tau}{n} \overline{p^n}, \quad \text{(B14)}$$

where we have introduced the shorthand

$$\overline{x^n} := \int x^n f(x) dx. \quad \text{(B15)}$$

Noting that the nth moment of the precipitation distribution (with $n \geq 1$) is given by

$$\overline{p^n} = (p_0)_n = p_0(p_0+1)\cdots(p_0+n-1), \quad \text{(B16)}$$

where p_0 is the average rainfall and $(p_0)_n$ is the (rising) Pochhammer symbol, the noncentral moments can now be computed using (B3) and (B16), such that

$$\overline{m} = \omega \zeta_1, \quad \text{(B17)}$$

$$\overline{m^2} = \omega \zeta_2 + \omega^2 \zeta_1^2, \quad \text{(B18)}$$

$$\overline{m^3} = \omega \zeta_3 + 3\omega^2 \zeta_1 \zeta_2 + \omega^3 \zeta_1^3, \quad \text{(B19)}$$

as desired.

REFERENCES

Axler, S., 1997: *Linear Algebra Done Right.* Undergraduate Texts in Mathematics, Springer, 251 pp., https://linear.axler.net/.

Bauer, A., and P. Carter, 2021: Existence of transonic solutions in the stellar wind problem with viscosity and heat conduction. *SIAM J. Appl. Dyn. Syst.*, **20**, 262–298, https://doi.org/10.1137/20M1314240.

Benson, D. O., and P. A. Dirmeyer, 2021: Characterizing the relationship between temperature and soil moisture extremes and their role in the exacerbation of heat waves over the contiguous United States. *J. Climate*, **34**, 2175–2187, https://doi.org/10.1175/JCLI-D-20-0440.1.

Best, M. J., and Coauthors, 2011: The Joint UK Land Environment Simulator (JULES), model description—Part 1: Energy and water fluxes. *Geosci. Model Dev.*, **4**, 677–699, https://doi.org/10.5194/gmd-4-677-2011.

Bieli, M., S. Pfahl, and H. Wernli, 2015: A Lagrangian investigation of hot and cold temperature extremes in Europe. *Quart. J. Roy. Meteor. Soc.*, **141**, 98–108, https://doi.org/10.1002/qj.2339.

Budyko, M. I., 1961: The heat balance of the Earth's surface. *Sov. Geogr.*, **2**, 3–13, https://doi.org/10.1080/00385417.1961.10770761.

Buzan, J. R., and M. Huber, 2020: Moist heat stress on a hotter earth. *Annu. Rev. Earth Planet. Sci.*, **48**, 623–655, https://doi.org/10.1146/annurev-earth-053018-060100.

Byrne, M. P., 2021: Amplified warming of extreme temperatures over tropical land. *Nat. Geosci.*, **14**, 837–841, https://doi.org/10.1038/s41561-021-00828-8.

——, and Coauthors, 2024: Theory and the future of land-climate science. *Nat. Geosci.*, **17**, 1079–1086, https://doi.org/10.1038/s41561-024-01553-8.

Carleton, T. A., and S. M. Hsiang, 2016: Social and economic impacts of climate. *Science*, **353**, aad9837, https://doi.org/10.1126/science.aad9837.

Chan, D., A. Rigden, J. Proctor, P. W. Chan, and P. Huybers, 2022: Differences in radiative forcing, not sensitivity, explain differences in summertime land temperature variance change between CMIP5 and CMIP6. *Earth's Future*, **10**, e2021EF002402, https://doi.org/10.1029/2021EF002402.

Copernicus Climate Change Service, 2019: ERA5-land monthly averaged data from 2001 to present. ECMWF, accessed 1 August 2021, https://doi.org/10.24381/CDS.68D2BB30.

Corless, R. M., G. H. Gonnet, D. E. G. Hare, D. J. Jeffrey, and D. E. Knuth, 1996: On the LambertW function. *Adv. Comput. Math.*, **5**, 329–359, https://doi.org/10.1007/BF02124750.

Dorigo, W., and Coauthors, 2017: ESA CCI soil moisture for improved earth system understanding: State-of-the art and future

directions. *Remote Sens. Environ.*, **203**, 185–215, https://doi.org/10.1016/j.rse.2017.07.001.

Duan, S. Q., K. A. McKinnon, and I. R. Simpson, 2024: Two perspectives on amplified warming over tropical land examined in CMIP6 models. *J. Climate*, **37**, 4743–4760, https://doi.org/10.1175/JCLI-D-22-0955.1.

Eagleson, P. S., 1978: Climate, soil, and vegetation: 2. The distribution of annual precipitation derived from observed storm sequences. *Water Resour. Res.*, **14**, 713–721, https://doi.org/10.1029/WR014i005p00713.

García-León, D., A. Casanueva, G. Standardi, A. Burgstall, A. D. Flouris, and L. Nybo, 2021: Current and projected regional economic impacts of heatwaves in Europe. *Nat. Commun.*, **12**, 5807, https://doi.org/10.1038/s41467-021-26050-z.

Gruber, A., W. A. Dorigo, W. Crow, and W. Wagner, 2017: Triple collocation-based merging of satellite soil moisture retrievals. *IEEE Trans. Geosci. Remote Sens.*, **55**, 6780–6792, https://doi.org/10.1109/TGRS.2017.2734070.

——, T. Scanlon, R. van der Schalie, W. Wagner, and W. Dorigo, 2019: Evolution of the ESA CCI soil moisture climate data records and their underlying merging methodology. *Earth Syst. Sci. Data*, **11**, 717–739, https://doi.org/10.5194/essd-11-717-2019.

Hasselmann, K., 1976: Stochastic climate models Part I. Theory. *Tellus*, **28**, 473–485, https://doi.org/10.1111/j.2153-3490.1976.tb00696.x.

Held, I. M., M. Winton, K. Takahashi, T. Delworth, F. Zeng, and G. K. Vallis, 2010: Probing the fast and slow components of global warming by returning abruptly to preindustrial forcing. *J. Climate*, **23**, 2418–2427, https://doi.org/10.1175/2009JCLI3466.1.

Hsu, H., and P. A. Dirmeyer, 2023: Soil moisture-evaporation coupling shifts into new gears under increasing CO_2. *Nat. Commun.*, **14**, 1162, https://doi.org/10.1038/s41467-023-36794-5.

Huybers, P., K. A. McKinnon, A. Rhines, and M. Tingley, 2014: U.S. daily temperatures: The meaning of extremes in the context of nonnormality. *J. Climate*, **27**, 7368–7384, https://doi.org/10.1175/JCLI-D-14-00216.1.

IPCC, 2021: *Climate Change 2021: The Physical Science Basis.* Cambridge University Press, 2392 pp.

Kong, Q., and M. Huber, 2023: Regimes of soil moisture–wet-bulb temperature coupling with relevance to moist heat stress. *J. Climate*, **36**, 7925–7942, https://doi.org/10.1175/JCLI-D-23-0132.1.

Koster, R. D., and M. J. Suarez, 2001: Soil moisture memory in climate models. *J. Hydrometeor.*, **2**, 558–570, https://doi.org/10.1175/1525-7541(2001)002<0558:SMMICM>2.0.CO;2.

——, and Coauthors, 2004: Regions of strong coupling between soil moisture and precipitation. *Science*, **305**, 1138–1140, https://doi.org/10.1126/science.1100217.

——, M. J. Suarez, and S. D. Schubert, 2006: Distinct hydrological signatures in observed historical temperature fields. *J. Hydrometeor.*, **7**, 1061–1075, https://doi.org/10.1175/JHM530.1.

Leach, N. J., and Coauthors, 2024: Heatwave attribution based on reliable operational weather forecasts. *Nat. Commun.*, **15**, 4530, https://doi.org/10.1038/s41467-024-48280-7.

Lorenz, R., E. B. Jaeger, and S. I. Seneviratne, 2010: Persistence of heat waves and its link to soil moisture memory. *Geophys. Res. Lett.*, **37**, L09703, https://doi.org/10.1029/2010GL042764.

Manabe, S., 1969: Climate and the ocean circulation I. The atmospheric circulation and the hydrology of the Earth's surface. *Mon. Wea. Rev.*, **97**, 739–774, https://doi.org/10.1175/1520-0493(1969)097%3C0739:CATOC%3E2.3.CO;2.

Martens, B., D. L. Schumacher, H. Wouters, J. Muñoz-Sabater, N. E. C. Verhoest, and D. G. Miralles, 2020: Evaluating the land-surface energy partitioning in ERA5. *Geosci. Model Dev.*, **13**, 4159–4181, https://doi.org/10.5194/gmd-13-4159-2020.

Mayer, J., M. Mayer, and L. Haimberger, 2021: Consistency and homogeneity of atmospheric energy, moisture, and mass budgets in ERA5. *J. Climate*, **34**, 3955–3974, https://doi.org/10.1175/JCLI-D-20-0676.1.

McColl, K. A., Q. He, H. Lu, and D. Entekhabi, 2019: Short-term and long-term surface soil moisture memory time scales are spatially anticorrelated at global scales. *J. Hydrometeor.*, **20**, 1165–1182, https://doi.org/10.1175/JHM-D-18-0141.1.

McKinnon, K. A., and I. R. Simpson, 2022: How unexpected was the 2021 Pacific Northwest heatwave? *Geophys. Res. Lett.*, **49**, e2022GL100380, https://doi.org/10.1029/2022GL100380.

——, ——, and A. P. Williams, 2024: The pace of change of summertime temperature extremes. *Proc. Natl. Acad. Sci. USA*, **121**, e2406143121, https://doi.org/10.1073/pnas.2406143121.

Meehl, G. A., and C. Tebaldi, 2004: More intense, more frequent, and longer lasting heat waves in the 21st century. *Science*, **305**, 994–997, https://doi.org/10.1126/science.1098704.

Mueller, B., and S. I. Seneviratne, 2012: Hot days induced by precipitation deficits at the global scale. *Proc. Natl. Acad. Sci. USA*, **109**, 12 398–12 403, https://doi.org/10.1073/pnas.1204330109.

Muñoz-Sabater, J., and Coauthors, 2021: ERA5-land: A state-of-the-art global reanalysis dataset for land applications. *Earth Syst. Sci. Data*, **13**, 4349–4383, https://doi.org/10.5194/essd-13-4349-2021.

Pastorello, G. Z., D. Papale, H. Chu, C. Trotta, D. A. Agarwal, E. Canfora, D. Baldocchi, and M. S. Torn, 2017: A new data set to keep a sharper eye on land-air exchanges. *Eos*, **98**, https://doi.org/10.1029/2017EO071597.

Patel, R. N., D. B. Bonan, and T. Schneider, 2024: Changes in the frequency of observed temperature extremes largely driven by a distribution shift. *Geophys. Res. Lett.*, **51**, e2024GL110707, https://doi.org/10.1029/2024GL110707.

Pfahl, S., and H. Wernli, 2012: Quantifying the relevance of atmospheric blocking for co-located temperature extremes in the Northern Hemisphere on (sub-)daily time scales. *Geophys. Res. Lett.*, **39**, L12807, https://doi.org/10.1029/2012GL052261.

Philip, S. Y., and Coauthors, 2022: Rapid attribution analysis of the extraordinary heat wave on the Pacific coast of the US and Canada in June 2021. *Earth Syst. Dyn.*, **13**, 1689–1713, https://doi.org/10.5194/esd-2021-90.

Proistosescu, C., A. Rhines, and P. Huybers, 2016: Identification and interpretation of nonnormality in atmospheric time series. *Geophys. Res. Lett.*, **43**, 5425–5434, https://doi.org/10.1002/2016GL068880.

Rhines, A., and P. Huybers, 2013: Frequent summer temperature extremes reflect changes in the mean, not the variance. *Proc. Natl. Acad. Sci. USA*, **110**, E546, https://doi.org/10.1073/pnas.1218748110.

Rice, J., 1977: On generalized shot noise. *Adv. Appl. Probab.*, **9**, 553–565, https://doi.org/10.2307/1426114.

Robine, J.-M., S. L. K. Cheung, S. L. Roy, H. Van Oyen, C. Griffiths, J.-P. Michel, and F. R. Herrmann, 2008: Death toll exceeded 70 000 in Europe during the summer of 2003. *C. R. Biol.*, **331**, 171–178, https://doi.org/10.1016/j.crvi.2007.12.001.

Santanello, J. A., Jr., and Coauthors, 2018: Land–atmosphere interactions: The LoCo perspective. *Bull. Amer. Meteor. Soc.*, **99**, 1253–1272, https://doi.org/10.1175/BAMS-D-17-0001.1.

Schaefer, G. L., M. H. Cosh, and T. J. Jackson, 2007: The USDA natural resources conservation Service Soil Climate Analysis

Network (SCAN). *J. Atmos. Oceanic Technol.*, **24**, 2073–2077, https://doi.org/10.1175/2007JTECHA930.1.

Schneider, T., T. Bischoff, and H. Płotka, 2015: Physics of changes in synoptic midlatitude temperature variability. *J. Climate*, **28**, 2312–2331, https://doi.org/10.1175/JCLI-D-14-00632.1.

Schumacher, D. L., J. Keune, C. C. van Heerwaarden, J. Vilà-Guerau de Arellano, A. J. Teuling, and D. G. Miralles, 2019: Amplification of mega-heatwaves through heat torrents fuelled by upwind drought. *Nat. Geosci.*, **12**, 712–717, https://doi.org/10.1038/s41561-019-0431-6.

Sellers, P. J., Y. Mintz, Y. C. Sud, and A. Dalcher, 1986: A Simple Biosphere Model (SIB) for use within general circulation models. *J. Atmos. Sci.*, **43**, 505–531, https://doi.org/10.1175/1520-0469(1986)043<0505:ASBMFU>2.0.CO;2.

——, and Coauthors, 1997: Modeling the exchanges of energy, water, and carbon between continents and the atmosphere. *Science*, **275**, 502–509, https://doi.org/10.1126/science.275.5299.502.

Seneviratne, S. I., D. Lüthi, M. Litschi, and C. Schär, 2006a: Land–atmosphere coupling and climate change in Europe. *Nature*, **443**, 205–209, https://doi.org/10.1038/nature05095.

——, and Coauthors, 2006b: Soil moisture memory in AGCM simulations: Analysis of Global Land–Atmosphere Coupling Experiment (GLACE) data. *J. Hydrometeor.*, **7**, 1090–1112, https://doi.org/10.1175/JHM533.1.

——, T. Corti, E. L. Davin, M. Hirschi, E. B. Jaeger, I. Lehner, B. Orlowsky, and A. J. Teuling, 2010: Investigating soil moisture–climate interactions in a changing climate: A review. *Earth-Sci. Rev.*, **99**, 125–161, https://doi.org/10.1016/j.earscirev.2010.02.004.

Sherwood, S. C., and M. Huber, 2010: An adaptability limit to climate change due to heat stress. *Proc. Natl. Acad. Sci. USA*, **107**, 9552–9555, https://doi.org/10.1073/pnas.0913352107.

Sippel, S., J. Zscheischler, and M. Reichstein, 2016: Ecosystem impacts of climate extremes crucially depend on the timing. *Proc. Natl. Acad. Sci. USA*, **113**, 5768–5770, https://doi.org/10.1073/pnas.1605667113.

Strogatz, S. H., 2018: *Nonlinear Dynamics and Chaos.* Vol. 1, 2nd ed. Westview Press, 528 pp.

Sun, Y., and Coauthors, 2024: Global supply chains amplify economic costs of future extreme heat risk. *Nature*, **627**, 797–804, https://doi.org/10.1038/s41586-024-07147-z.

Tamarin-Brodsky, T., K. Hodges, B. J. Hoskins, and T. G. Shepherd, 2020: Changes in Northern Hemisphere temperature variability shaped by regional warming patterns. *Nat. Geosci.*, **13**, 414–421, https://doi.org/10.1038/s41561-020-0576-3.

Teuling, A. J., S. I. Seneviratne, C. Williams, and P. A. Troch, 2006: Observed timescales of evapotranspiration response to soil moisture. *Geophys. Res. Lett.*, **33**, L23403, https://doi.org/10.1029/2006GL028178.

Trugman, A. T., D. Medvigy, J. S. Mankin, and W. R. L. Anderegg, 2018: Soil moisture stress as a major driver of carbon cycle uncertainty. *Geophys. Res. Lett.*, **45**, 6495–6503, https://doi.org/10.1029/2018GL078131.

Van Loon, S., and D. W. J. Thompson, 2023: Comparing local versus hemispheric perspectives of extreme heat events. *Geophys. Res. Lett.*, **50**, e2023GL105246, https://doi.org/10.1029/2023GL105246.

Vargas Zeppetello, L. R., and D. S. Battisti, 2020: Projected increases in monthly midlatitude summertime temperature variance over land are driven by local thermodynamics. *Geophys. Res. Lett.*, **47**, e2020GL090197, https://doi.org/10.1029/2020GL090197.

——, ——, and M. B. Baker, 2019: The origin of soil moisture evaporation "regimes". *J. Climate*, **32**, 6939–6960, https://doi.org/10.1175/JCLI-D-19-0209.1.

——, ——, and ——, 2022: The physics of heat waves: What causes extremely high summertime temperatures? *J. Climate*, **35**, 2231–2251, https://doi.org/10.1175/JCLI-D-21-0236.1.

Whan, K., J. Zscheischler, R. Orth, M. Shongwe, M. Rahimi, E. O. Asare, and S. I. Seneviratne, 2015: Impact of soil moisture on extreme maximum temperatures in Europe. *Wea. Climate Extremes*, **9**, 57–67, https://doi.org/10.1016/j.wace.2015.05.001.

Zhang, Y., and W. R. Boos, 2023: An upper bound for extreme temperatures over midlatitude land. *Proc. Natl. Acad. Sci. USA*, **120**, e2215278120, https://doi.org/10.1073/pnas.2215278120.

——, I. Held, and S. Fueglistaler, 2021: Projections of tropical heat stress constrained by atmospheric dynamics. *Nat. Geosci.*, **14**, 133–137, https://doi.org/10.1038/s41561-021-00695-3.